



POLITEHNICA UNIVERSITY OF BUCHAREST

**Doctoral School of Engineering and Applications of Lasers
and Accelerators**

Decision No. from

PH.D. THESIS SUMMARY

Anamaria SPĂTARU

MĂSURĂTORI DE MASĂ CU ACURATEȚE RIDICATĂ PENTRU NUCLEELE
BOGATE ÎN NEUTRONI ȘI STUDIUL TRANZIȚIEI DE FAZĂ PENTRU $N = 90$

HIGH-ACCURACY MASS MEASUREMENTS OF NEUTRON RICH NUCLEI
AND STUDY OF $N = 90$ SHAPE PHASE TRANSITION

THESIS COMMITTEE

Prof. Dr. Ing. Calin A. UR Politehnica Univ. of Bucharest	President
Prof. Dr. Dimiter L. BALABANSKI Politehnica Univ. of Bucharest	PhD Supervisor
Prof. Dr. Gheorghe CĂȚA-DANIL Politehnica Univ. of Bucharest	Referee
Prof. Dr. Israel MARDOR Tel Aviv University	Referee
Prof. Dr. Mihaela SIN University of Bucharest	Referee

BUCHAREST 2022

Acknowledgements

I would like to offer my thanks and appreciation to all the people that helped me during the last five years and made this work possible.

I'm extremely grateful to my supervisors Prof. Dr. Dimiter L. Balabanski and Dr. Paul Constantin for their patience in answering all my questions and constant feedback throughout my work. I am also grateful to the members of the guidance committee Prof. Dr. Ing. Calin A. Ur, Prof. Dr. Octavian Sima and Dr. Catalin Matei who offered me important advises.

Many thanks to my colleagues from ELI-NP: Andreea Gherghe, Teodora Madgearu, Dragos Nichita, Dr. Adrian Rotaru and Alexandru State with whom I worked together and also spent lunch breaks with fruitful discussions. Thanks should also go to all past and present members of the Gamma Driven Experiments Department.

This journey would have not been possible without the Fragment Separator - Ion Catcher group at GSI, who introduced me to the field of experimental nuclear physics, especially Prof. Dr. Christoph Scheidenberger, Dr. Timo Dickel and Dr. Wolfgang R. Plaß. I would like to extend my sincere thanks to my colleagues at GSI: Daler Amanbayev, Dr. Samuel Ayet San Andrés, Dr. Sönke Beck, Julian Bergmann, Lizzy Gröf, Dr. Christine Hornung, Gabriella Kripko- Koncz and Dr. Ivan Miskun.

I am also thankful to our secretaries, Simona Niculae and Ewa Tracz, who were always kind to help me with all the complicated paperwork for my travels and work.

I would also like to thank my parents and sister, who supported me from the beginning and offered me a calm environment after a long day of work. I would be remiss in not mentioning my cat, Atomită, whom I missed very much during my travels to GSI. Special thanks to Florian, who listened to all my complains and offered me the moral support I needed.

Last but not least I would like to thank to everybody that was involved in the work presented in my thesis but was not mentioned specifically.

Table of contents

1	Introduction	1
2	Reactions for production of neutron-rich nuclei	2
2.1	Fragmentation reaction	2
2.2	Nuclear Fission	3
2.2.1	Spontaneous fission	3
2.2.2	Induced fission	3
2.3	Multi-Nucleon Transfer	4
2.4	Summary	4
3	Principles of mass separation and measurements	5
3.1	Mass separation	5
3.1.1	Magnetic elements	5
3.1.2	Radio Frequency Quadrupoles	6
3.2	Indirect measurement methods	7
3.2.1	Nuclear decays	7
3.2.2	Nuclear reactions	7
3.3	Direct measurement methods	8
3.3.1	Penning Trap	8
3.3.2	Storage rings	8
3.4	Time-of-flight mass spectrometers	9
3.4.1	FRS and FRS-IC	9
3.5	Summary	10
4	Shape-phase transition	11
4.1	Nuclear shapes and nuclear structure models	11
4.2	Shape-transitions	12
4.2.1	Excited state observables	12
4.2.2	Ground state observables	13
4.3	Summary	13
5	Data Acquisition systems	15
5.1	FRS and FRS-IC DAQ coupling	15
5.2	Measurement calibration and accuracy	15
5.3	Improved signal-to-noise ratio based on spill structure	17

5.4	On-line monitoring	17
5.5	Improved signal-to-noise ratio by event correlation	18
5.6	Summary	18
6	Fission fragment measurements and mass evaluation at the FRS-IC	19
6.1	Experimental setup and measurements	19
6.2	Data evaluation procedure	19
6.2.1	Conversion to mass spectrum and calibration	20
6.2.2	Determination of the peak shape	20
6.2.3	Mass and uncertainty determination	21
6.2.4	Averaging method for several independent measurements	23
6.2.5	Fission fragments calibration results	24
6.3	Summary	24
7	Mass measurements and shape-phase transition at N = 90	25
7.1	Experimental results	25
7.2	Discussion	25
7.3	Summary	26
8	Heavy Neutron-Rich Isotope Production via Multi-Nucleon Transfer Reactions	27
8.1	Experimental programs at the FRS-IC and IGISOL	27
8.2	Process and setup implementation in GEANT4	28
8.3	Simulation with the FRS-IC setup	29
8.3.1	Results using GRAZING model	29
8.3.2	Results using Langevin-type model	31
8.4	Measurements and simulations using the IGISOL setup	31
8.5	Summary	32
9	Summary and Outlook	33
	Appendix List of figures	34
	References	38

Chapter 1

Introduction

Nuclear mass is one of the basic measurable quantities of nuclei, which provides information on their inner structure and the interaction between their constituents (i.e. protons and neutrons). The study of masses from neutron-rich nuclei is extending our knowledge in fields such as: nuclear astrophysics (by understanding the origin and the production methods of the nuclei during the primordial and stars nucleosynthesis), nuclear structure (the study of nuclear binding energies gives information on the limits of nuclear stability and the possibilities of decay) and theory (describing the properties of the nucleus and predicting binding energies where measurements are not available).

The present work is focusing on the improvements in nuclear structure that can be performed by measuring masses at $A \sim 150$, in particular the study of the transition between two nuclear shapes. For this purpose, the Fragment Separator (FRS) and FRS-Ion Catcher (FRS-IC) setups at GSI, Darmstadt are used to perform mass measurements via time-of-flight mass spectrometry. As a first step, an improvement to the data acquisition system of FRS is done in order to allow further for accurate mass selection and determination. For the first time in an experimental campaign, using a ^{252}Cf spontaneous fission source, almost 70 nuclei were measured simultaneously. This result opens the possibility for further measurements of the relative cross sections using the gas-cell technique. Based on this measurement results the shape transition at $N = 90$ are studied and compared with theoretical calculations. Further studies using heavier nuclei are considered using investigation of the multinucleon transfer (MNT) reaction. This mechanism has shown to produce neutron-rich nuclei with higher cross-section than the fragmentation reaction [1]. The study presented in this thesis is focusing on the possibility of using the MNT reactions at two facilities, FRS-IC and Ion Guide Isotope Separator On-Line facility at JYFL Accelerator Laboratory.

Chapter 2

Reactions for production of neutron-rich nuclei

The neutron-rich nuclei located close to the edge of the nuclear chart are showing characteristics of high importance for studies of the nuclear structure and nucleosynthesis, as detailed in Chapter 1. However, their production and study are a challenge for experiments around the world because of their small production cross sections and half lives. In this chapter are described three mechanisms used in the production of neutron-rich nuclei.

2.1 Fragmentation reaction

Fragmentation is a peripheral nuclear reaction that takes place at relativistic energies and produces neutron-rich nuclei in the region below the projectile nucleus. It is usually described as a two step reaction in which several nucleons are removed during the interaction and afterwards several other nucleons are evaporated due to the increased excitation energy. One of the models used to theoretically describe the reaction is the abrasion-ablation model discussed in details in Ref. [2]. The process is shown schematically in Fig. 2.1.

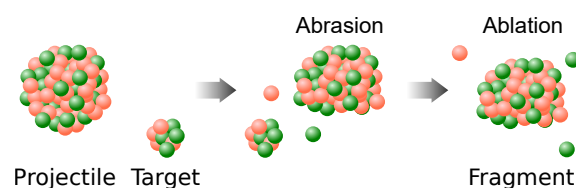


Fig. 2.1 Schematic representation of the fragmentation reaction mechanism from a point of view of the abrasion-ablation model.

The momentum of the final fragments plays an important role in understanding the reaction mechanism. The calculation of the width of the longitudinal momentum $\sigma_{p_{||}}$, Eq. 2.1, connects the mass numbers of the projectile, A_P , the abraded fragment, A_F and the momentum of the Fermi motion, p_F [3].

$$\sigma_{p_{||}}^2 = \frac{p_F^2}{5} \cdot \frac{A_F(A_P - A_F)}{A_P - 1} \quad (2.1)$$

2.2 Nuclear Fission

Nuclear fission is a process in which neutron rich nuclei are generated in the splitting of a heavy (mother) nucleus into preferentially two fragments with release of energy, neutrons and gamma rays. Some nuclei undergo fission without an external help, process known as spontaneous fission. The fragments generated as a result of nuclear fission have predominantly an asymmetric mass distribution (generation of a low and a complementary high mass fragment) caused by shell effects.

2.2.1 Spontaneous fission

^{252}Cf is one of the nuclei which undergoes spontaneous fission and is frequently used as a source for production and studies of neutron-rich nuclei. It has a half life of 2.647 years and a branching ratio for the spontaneous fission of 3.102% [4], which provides easily a high rate of fission events.

2.2.2 Induced fission

Nuclear fission can be induced in nuclear reactions using both direct and inverse kinematics. The direct kinematics technique, shown schematically in the upper part of Fig. 2.4, will allow high resolution measurement of the fission resonances and an increased fission yields.

In inverse kinematics the projectile can be generated from a different reaction, such as it is the case of the abrasion-fission, when the fragmentation and fission reactions are combined, see middle panel of Fig. 2.4. Another unique mechanism is the Coulomb-fission, shown schematically in the bottom part of Fig. 2.4.

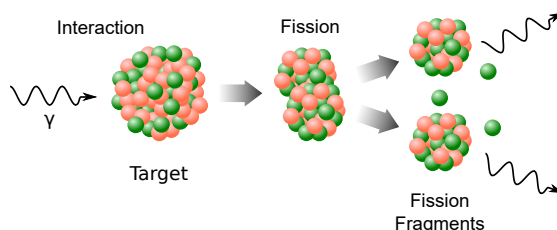


Fig. 2.2 Photofission reaction uses photons to excite nuclei to precise energies above the fission barrier.

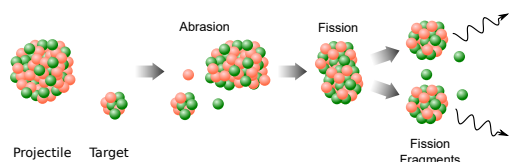


Fig. 2.3 Abrasion-fission is the process in which at small impact parameters a nucleus abrades after the interaction with a light target. As a consequence the nucleus is left excited and undergoes fission.

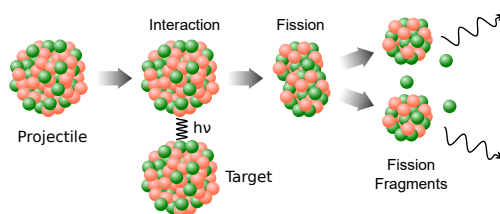


Fig. 2.4 Coulomb-fission is the process in which a nucleus gets excited and undergoes fission after the exchange of a virtual photon (indicated as $h\nu$ in the cartoon).

2.3 Multi-Nucleon Transfer

The process of multi-nucleon transfer (MNT) assumes that for low energies of the incoming nucleus (kinetic energy only slightly above the Coulomb barrier) and an impact parameter as for peripheral collisions (i.e. \lesssim sum of the two nuclei radiuses), the incident particle interacts with the target by forming a deformed system with an excited neck structure. In the evolution of such systems, neutrons and protons are exchanged between the two initial particles. As the excitation energy is consumed, fragments separate without the formation of a compound nucleus. The process is schematically represented in Fig. 2.5. Recent experiments [1] show that MNT reaction is a promising path for the production of neutron-rich nuclei at the $N = 126$ abundance distribution peak.

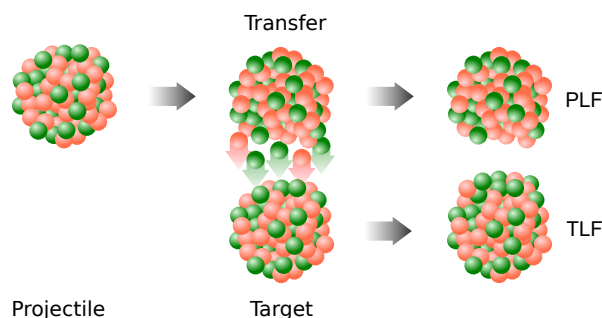


Fig. 2.5 During the multinucleon-transfer reactions the projectile and the target nuclei interact without the formation of a compound nucleus and exchange several nucleons, leading to the formation of a Projectile-like-Fragment (PLF) and Target-like-Fragment (TLF).

GRAZING and Langevin-type model characteristics and comparison

The theoretical studies of Winther [5] for the MNT reaction in deep inelastic grazing collisions were implemented in the simulation code GRAZING. It is the main simulation tool used for such reactions using a semi-classical approach. However, nuclear deformations and fissioning of the resulting reaction products are not taken into account. The Langevin-type model [6, 7] simulates the continuous evolution of a colliding system of nuclei, starting with their approach, the formation of the mononuclear system and the separation of the decay products.

In the particular case of the reaction $^{64}\text{Ni} + ^{238}\text{U}$ at $E_{lab} = 390$ MeV, experimental data of the isotopic distributed cross-sections can be found in Ref. [8]. Therefore, it facilitates the comparison between the model previously described, the GRAZING model and the experimental observations.

2.4 Summary

This comparison between the GRAZING, Langevin-type models for MNT reactions and the experimental data available is part of the following publications: A. Spătaru et al., *Multi-Nucleon Transfer reactions in $^{238}\text{U} + ^{64}\text{Ni}$ using Grazing model*, U.P.B. Sci. Bull., Series A, Vol. 82, Iss. 1, 2020, A. Spătaru et al., *Multi-Nucleon Transfer studies of ^{238}U induced reactions on ^{64}Ni , ^{164}Dy and ^{209}Bi targets using a Langevin-type model*, in progress

Chapter 3

Principles of mass separation and measurements

The atomic mass, or the binding energy, is a key property of the ground state of nuclei, see Eq. 3.1, where the following notations were used for the masses of protons - Zm_p , neutrons - Nm_n and electrons - Zm_e and nuclear binding energy, $B(A,Z)$, and the electron binding energy, $B_e(Z)$.

$$M_{atomic}(A, Z) = Zm_p + Nm_n - B(A, Z)/c^2 + Zm_e - B_e(Z)/c^2 \quad (3.1)$$

This chapter presents the basic theoretical aspects for determining the atomic mass using both indirect and direct methods.

3.1 Mass separation

The precise mass measurements of exotic nuclei often require their separation from other ionic species produced in the same reaction before the actual measurement can take place. A common solution is the usage of ion beam optics elements inside the beam line. In case of low energy beamlines a common source of impurities are molecules. A solution for reducing the contamination by breaking up molecules is based on Collision Induced Dissociation (CID). A procedure that uses CID [9] in combination with the mass selectivity of Radio Frequency Quadrupoles (RFQs) was implemented at the FRS-IC setup at GSI.

3.1.1 Magnetic elements

In the presence of a magnetic field, B , an ion of mass, m , and charge, q , having a velocity, v , perpendicular to the field direction will follow a circular path of radius, r , case in which the magnetic force is expressed based on the centripetal acceleration, Eq.3.2 [10].

$$qvB = \frac{mv^2}{r} \rightarrow \frac{m}{q} = \frac{r^2 B^2}{2U} \quad (3.2)$$

The mass resolving power of a pure magnetic element is limited. To increase its ability of separating masses, the energy dispersion needs to be compensated. This can be done by adding an electrostatic sector. It consists out of two curved plates to which an equal voltage with opposite

polarity is supplied, generating an electric field of intensity E . The energy dispersion of the electrostatic sector can be seen in Eq. 3.3.

$$qE = \frac{mv^2}{r} \rightarrow r = \frac{mv^2}{qE} \quad (3.3)$$

3.1.2 Radio Frequency Quadrupoles

Quadrupoles are composed out of four rod electrodes of radius r_0 placed parallel one to another in a square-like configuration. A combination of radio frequency (RF) and direct current (DC) fields are applied to the two pairs of opposite rods. A positive ion traveling along the space between the rods will feel the total field, Φ_0 , made out of the DC potential (U), RF potential (V) and angular frequency, ω , Eq. 3.4 [10].

$$\Phi_0 = U + V \cos \omega t \quad (3.4)$$

The movement of the ions is described by the equation of motion, Eq. 3.5 [11], for $u = x$ or $u = y$, based on the potential shown in Eq. 3.4 and considering $\xi = \omega t/2$.

$$\frac{d^2 u}{d\xi^2} = - \left(\frac{8qU}{m\omega^2 r_0^2} + \frac{8qV \cos(2\xi)}{m\omega^2 r_0^2} \right) \cdot u \quad (3.5)$$

This is a Mathieu type equation for which the solution is known, see Ref. [12]. The Mathieu parameters are defined as in Eq. 3.6.

$$\begin{aligned} a_x = -a_y &= \frac{8qU}{m\omega^2 r_0^2} \\ q_x = -q_y &= \frac{4qV}{m\omega^2 r_0^2} \end{aligned} \quad (3.6)$$

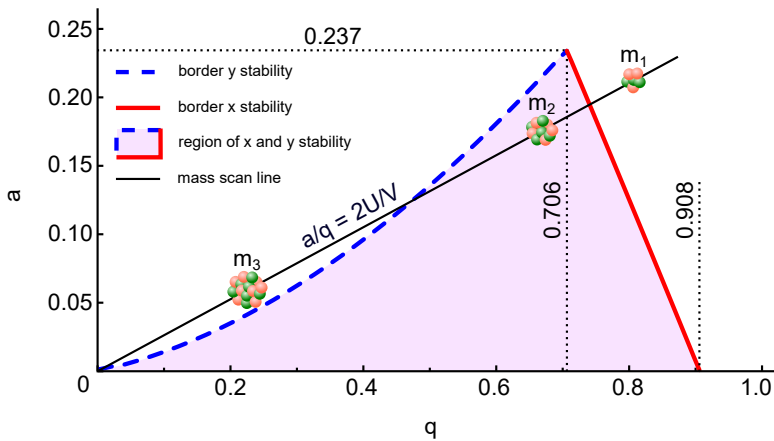


Fig. 3.1 First region of the stability diagram as function of the Mathieu parameters. Only mass m_2 lies inside the stability borders, shown in pink, and can be transmitted. The apex of the region is at $a = 0.237$ and $q = 0.706$ and is representing the point where the mass filter would transport only one mass.

To successfully transport ions through the system, they must have a stable trajectory around its center such that the ions are not lost by hitting the rods. This requirement is fulfilled for a U/V ratio specific for each m/q . For a fix value of the U/V , the quadrupole system will act as a mass filter, allowing to one type of ions of mass m/q to have a stable trajectory.

The Mathieu parameters, $a_{x,y}$ and $q_{x,y}$ Eq. 3.6, are used to link the masses of the ions to the DC and RF potentials applied to the RFQ rods.

3.2 Indirect measurement methods

One way of determining the atomic mass is through measurements of the energy released in a nuclear reaction or decay (Q). It is calculated as the difference between the masses of the initial ions ($m_{initial}$) and the ones of the final products (m_{final}), $Q=(m_{initial}-m_{final})c^2$.

3.2.1 Nuclear decays

In a nuclear decay, the initial nucleus at rest, denoted in Eq. 3.7 with A , is spontaneously decreasing its mass to a more stable configuration often referred to as daughter nucleus, B , by the emission of one or more particles, denoted here by b and c . The energy released in decay (Q), as shown in Eq. 3.8, is linking the masses of the initial and final products of a decay.

$$A \rightarrow B + b + c \quad (3.7)$$

$$\begin{aligned} Q &= (M_A(A, Z) - M_B(A, Z - 2) - m_b - m_c)c^2 \\ &= E_{Kin,B} + E_{Kin,b} + E_{Kin,c} \end{aligned} \quad (3.8)$$

The released energy can be written in terms of the kinetic energy of the helium nucleus, $E_{Kin,\alpha}$, its mass, m_α , and the mass of the daughter nucleus, $m_{daughter}$. Eq. 3.9 allows for the Q determination from measurements of $E_{Kin,\alpha}$.

$$Q = E_{Kin,\alpha} \left(1 + \frac{m_\alpha}{m_{daughter}} \right) \quad (3.9) \quad Q = E_{endpoint} \left(1 + \frac{m_\beta}{m_{daughter}} \right) + E_\gamma \quad (3.10)$$

Eq. 3.10 gives the relationship between the energy released in the β_- , β_+ decays or the electron capture (EC) and the mass of the generated daughter ion ($m_{daughter}$), where with E_γ is denoted the energy of the γ -ray emitted when the daughter ion is in an excited state and $E_{endpoint}$ is the upper energy limit of the continuous energy spectrum emitted during the decay.

3.2.2 Nuclear reactions

Another method for atomic mass determination is by using nuclear reactions. In a nuclear reaction a moving projectile, A , interacts with a target ion at rest, B , and generates new products, denoted by C and D .

$$A + B \rightarrow C + D \quad (3.11)$$

The energy released in a nuclear reaction ($Q_{reaction}$) is calculated from the difference between the mass of the incoming nuclei and the one of the final products, Eq. 3.12.

$$Q_{reaction} = (M_A + M_B - M_C - M_D)c^2 \quad (3.12)$$

The reactions which generated two final products are studied using the missing mass method or the invariant mass method.

3.3 Direct measurement methods

The direct determination of atomic masses can be performed using different methods which involve the motion of particles in electric and/or magnetic fields.

3.3.1 Penning Trap

Penning Traps are devices that perform highly accurate mass measurements by storing the ions in a combined magnetic and electric field. The movement of the ion is characterized by three independent motions: axial (ω_z), modified cyclotron (ω_+) and magnetron (ω_-). Their measurement is used for mass determinations through calculation of the cyclotron frequency (ω_C), Eq. 3.13 [13]. Fig. 3.13 illustrates the three motions separately and the resulted motion of their combination. The mass determination can be done using the time of flight method [14] and the Fourier Transform Ion Cyclotron Resonance method [15].

$$\omega_C = \left(\frac{q}{m}\right) B = \sqrt{\omega_+^2 + \omega_-^2 + \omega_z^2} \quad (3.13)$$

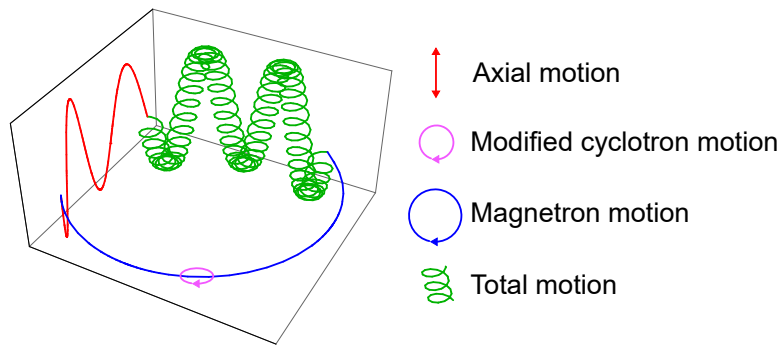


Fig. 3.2 Schematic representation of the three oscillations (defined in the legend of the figure) which are describing the motion of the ions inside a Penning Trap.

3.3.2 Storage rings

Storage rings are large (> 100 m in circumference) and complex devices that use the revolution frequencies (Schottky Mass Spectrometry, SMS) or revolution times (Isochronous Mass Spectrometry, IMS) of the ions in a closed path to perform mass measurements. The revolution frequency, f , and the revolution time, T , is related to the mass-over-charge, m/q , as in Eq. 3.14

[16].

$$\frac{\Delta f}{f} = -\frac{\Delta T}{T} = -\frac{1}{\gamma_t^2} \frac{\Delta(m/q)}{(m/q)} + \left(1 - \frac{\gamma^2}{\gamma_t^2}\right) \frac{\Delta v}{v} \quad (3.14)$$

Here, γ_t is the transition point at which the frequency is independent on the velocity, β introduces the ratio between the particle velocity and the velocity of light in vacuum and γ denotes the relativistic Lorentz factor (i.e. $\gamma = 1/\sqrt{1-\beta^2}$).

3.4 Time-of-flight mass spectrometers

The time-of-flight mass spectrometers (ToF-MS) are devices that deduce the m/q using measurements of the ions time-of-flight over a closed path [17]. In present they can reach resolving powers close to 10^6 and accuracies of 10^{-8} [18].

Starting with a bunch of ions of different masses at the same kinetic energy that are traveling on a fixed distance (D) under the influence of an electric field (U), their flight times (t) will be distributed directly proportional to $\sqrt{m/q}$. This observation is expressed mathematically in Eq. 3.15, where the experimental constants were denoted by $a = \frac{2U}{D^2}$. This equation represents the fundamental principle of the TOF-MS.

$$\frac{m}{q} = \frac{2U}{D^2} \cdot t^2 = a \cdot t^2 \quad (3.15) \quad R = \frac{(m/q)}{\Delta(m/q)} = \frac{t}{2\Delta t} \quad (3.16) \text{ The re-}$$

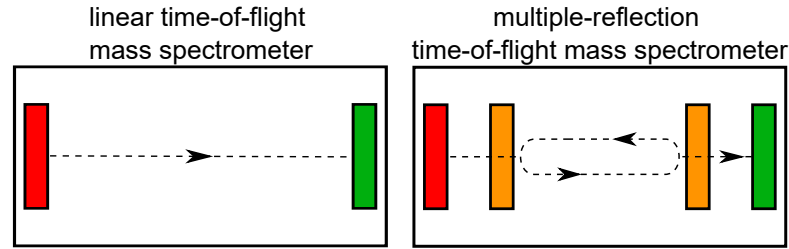


Fig. 3.3 Representation of the linear (upper figure) and multiple reflection (bottom figure) mass spectrometers. The injection plate and the detector are shown in red and green, respectively. With orange are represented the reflecting mirrors used to increase the flight distance.

solving power can be calculated from both m/q and t and the corresponding FWHM of the measured peaks ($\Delta(m/q)$ or Δt), Eq. 3.16. The increase of the resolving power can be done by increasing the traveling distance and consequently the flight time. In Fig. 3.3 there are shown schematically the linear and the closed-path multiple-reflection ToF-MS.

3.4.1 FRS and FRS-IC

The FRagment Separator (FRS) is a magnetic spectrometer having four magnetic dipole stages for transport and separation of ions and a set of Particle IDentification (PID) detectors for identification and analysis. A schematic drawing of the FRS and the FRS-Ion Catcher (FRS-IC) setup is shown in Fig. 3.4. A resulting particle identification plot as performed with the FRS is shown in the top part of Fig. 3.5, having a resolution of $\sigma_Z = 0.16$ and $\sigma_{A/Q} = 0.003$.

The FRS-IC setup has three main components: a gas-filled Cryogenic Stopping Cell (CSC) [19, 20], a radio frequency quadrupole (RFQ) [21, 22] beamline and a Multiple Reflection Time-of-Flight Mass Spectrometer (MR-ToF-MS) [23]. It provides information on the mass-to-charge

ratio of the ions using an MR-ToF-MS approach [24]. Such a high-resolution mass spectrometer allows for a full identification using only the measured mass-to-charge ratio [25].

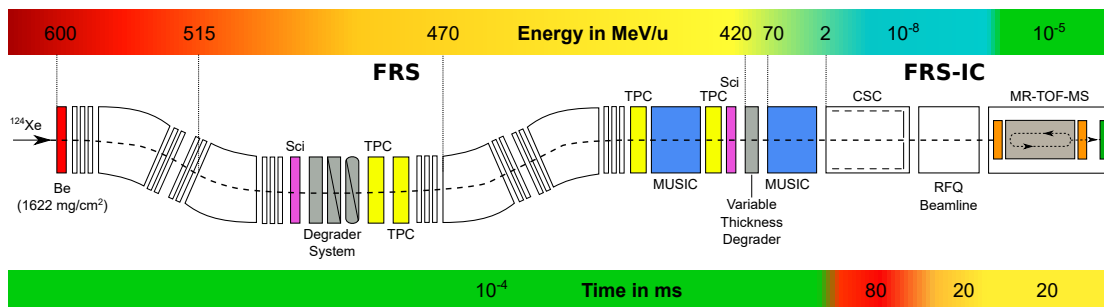


Fig. 3.4 Schematic drawing of the FRS [26] and FRS-IC [27] setups. The set of SCI [28], TPC [29] and MUSIC [30, 31] detectors provides the FRS PID, also referred to as identification before the CSC, while the MR-ToF-MS provides by a precision mass measurement the identification after the CSC. Above the corresponding energies in the experimental setup are shown. Below the flight times in the different sections are indicated.

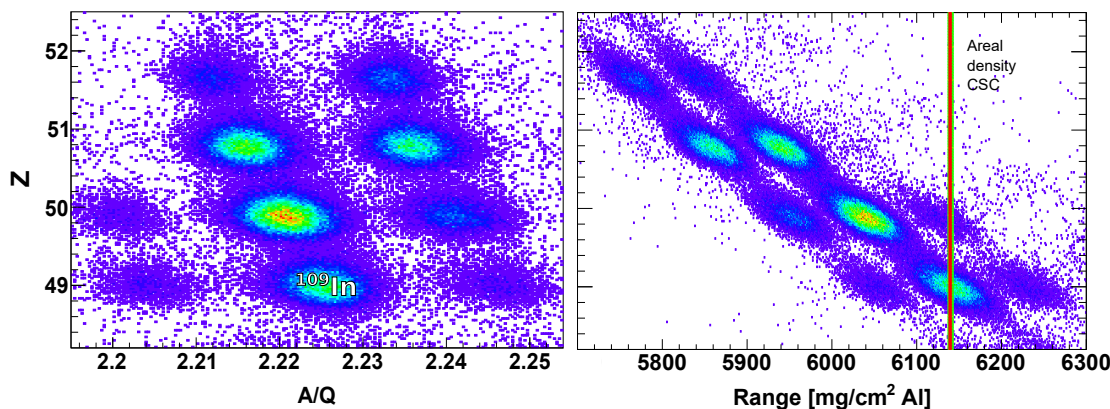


Fig. 3.5 Example of an FRS PID plot in which the system was optimized for the measurement of ^{109}In (upper figure). Range distribution at the final focal plane in Al of ions in the FRS PID (lower figure). The calculation is based on fits to data [32]. The areal density and the position of the CSC in range is marked with in red.

3.5 Summary

The description of the FRS and FRS-IC setup presented in this Chapter is included in the following publication: A. Spătaru et al., *First coupling of the FRS particle identification and the FRS-Ion Catcher data acquisition systems: The case of ^{109}In* , Nucl. Instr. and Meth. in Phys. Res. B 522, 2022

Chapter 4

Shape-phase transition

Throughout the nuclear chart, nuclei have shown to possess different shapes (i.e. spherical or deformed), based on the number of their protons and neutrons. By studying the transition points between two nuclear shapes important information is gained on the interaction between nucleons, which is further used to develop nuclear models.

This chapter introduces the basic aspects of the shell and collective models which describe the spherical and deformed shapes of the nuclei. The transition points between the nuclear shapes are discussed using studies from the observables of the excited states as well as ground states of the nuclei.

4.1 Nuclear shapes and nuclear structure models

A large number of the nuclei have deformed shapes with an axial symmetry, while at specific proton and neutron number, commonly referred to as magic numbers (e.g. $Z, N = 2, 8, 20, 28, 50, 82, 126$, etc.) the nuclei display a spherical shape. In Fig. 4.1 are schematically represented the spherical and the most common symmetrical deformed shapes.

The surface deformations are described in Eq. 4.1 using the spherical harmonics ($Y_{\lambda\mu}(\theta, \phi)$) and an amplitude ($\alpha_{\lambda\mu}$), which defines the deformation, added to the radius of the spherical nucleus, R_0 . When the deformation parameters $\alpha_{\lambda\mu} = 0$, the nucleus has a spherical shape.

$$R(\theta, \phi) = R_0 \left[1 + \sum_{\lambda \geq 1} \sum_{\mu = -\lambda}^{-\lambda} \alpha_{\lambda\mu} Y_{\lambda\mu}(\theta, \phi) \right] \quad (4.1)$$

Nuclear models are offering a simplified perspective over the structure of the atomic nucleus. The nuclear shell model [33, 34] is one of the first approaches to establish a nuclear model, which has shown to successfully characterize spherical nuclei. The deformed shell model, also known as Nilsson model [35] considers the changing shape of the nucleus, as it is described in Eq. 4.1.

Medium-heavy and heavy nuclei display characteristics which could not be explained in the frame of the shell or Nilsson model (e.g. the smooth decrease of the energy of the first excited state as a function of the mass number). The observations were described by the influence of the collective motion of the nucleons: the nuclear vibrations and rotations.

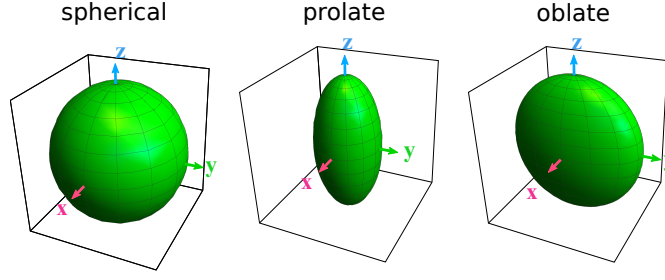


Fig. 4.1 Schematic representation of the spherical nuclear shape and the two deformed prolate and oblate shapes.

4.2 Shape-transitions

The transitional behavior of nuclei is analyzed theoretically using the Interacting Boson Model (IBM) [36]. The model is considering transitions between the three collective behavior shapes, which are classified in two groups: first-order phase transition (transition from spherical shape to axially deformed shape) and second-order phase transition (transition from spherical shape to deformed shape with γ -instability) [37].

From microscopic considerations, the transition between a spherical to a deformed shape is connected to the interaction between valence nucleons.

4.2.1 Excited state observables

Measurements of the excited state observables such as the energy of the first excited state and its quadrupole moments were the first ones to display characteristics of the nuclear collective properties.

The energy ratio between the first 4_1^+ state, $E(4_1^+)$, and the first 2_1^+ state, $E(2_1^+)$, Eq. 4.2 exhibits regular patterns with sharp changes at critical points. In Fig. 4.2 the ratio is calculated for the even-even nuclei with $Z = 56 - 66$ and above the $N = 82$ closed shell. This region is typical for the transition between $R_{4/2} \approx 2$ and $R_{4/2} \approx 3$, which in some nuclei (e.g. Sm, Gd, Dy) is rather sharp, indicating the shape phase transition.

$$R_{4/2} = \frac{E(4_1^+)}{E(2_1^+)} \quad (4.2)$$

A second parameter, which is used as an indicator of the shape phase transition, involves the strength of the electric quadrupole (E2). The ratio $B_{4/2}$ (defined in Eq. 4.3) is indicating the shape transition region by showing decreasing values, e.g. $B_{4/2} = 2$ in the region of the spherical nucleus and $B_{4/2} = 1.4$ in the region of the deformed nucleus.

$$B_{4/2} = \frac{B(E2; 4_1^+ \rightarrow 2_1^+)}{B(E2; 2_1^+ \rightarrow 0_1^+)} \quad (4.3)$$

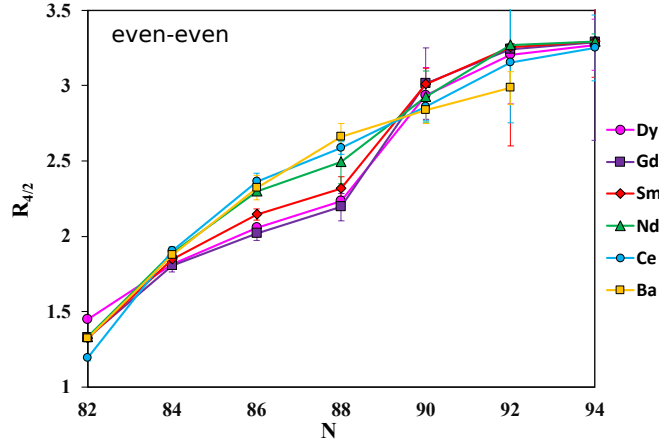


Fig. 4.2 Ratio between the energy of the first 4^+ and 2^+ excited states around the $N = 90$ critical point for nuclei with an even number of protons and neutrons. Data from <https://www.nndc.bnl.gov/ensdf/>

4.2.2 Ground state observables

The nuclear binding energy, $B(Z, N)$, is defined in Eq. 4.4 for a nucleus with nuclear mass $M(Z, N)$ and according to the notations in Chapter 3.

$$B(Z, N) = [Z \cdot m_p + N \cdot m_n - M(Z, N)] \cdot c^2 \quad (4.4)$$

The two neutron separation energy, S_{2n} (Eq. 4.5), provides more details on the characteristics of the nuclear structure.

$$S_{2n}(Z, N) = B(Z, N) - B(Z, N - 2) \quad (4.5)$$

In the upper part of Fig. 4.3 is shown the trend of the S_{2n} over the neutron number for even-even nuclei above the $N = 82$ closed shell. The deviations seen in the chains of neodymium, samarium and gadolinium are emphasized with a dashed circle in Fig. 4.5. This effect is indicating the transition region between the spherical to deformed shapes (i.e. first order phase transition).

$$dS_{2n}(Z, N) = \frac{S_{2n}(Z, N + 2) - S_{2n}(Z, N)}{2} \quad (4.6)$$

The first derivative of the two neutron separation energy is a second parameter that is used in the studies of nuclear shape change through mass measurements, Eq. 4.6. In the bottom part of Fig. 4.3 and Fig. 4.4 are shown the trends of the dS_{2n} for the even-even and even-odd nuclei at $N = 90$

4.3 Summary

The evolution of the S_{2n} and dS_{2n} for nuclei with $N = 90$ represents the physics case of a forthcoming publication: A. Spătaru et al., *Accurate mass measurements near the $N=90$ shape phase transition region at the FRS-IC*, in progress

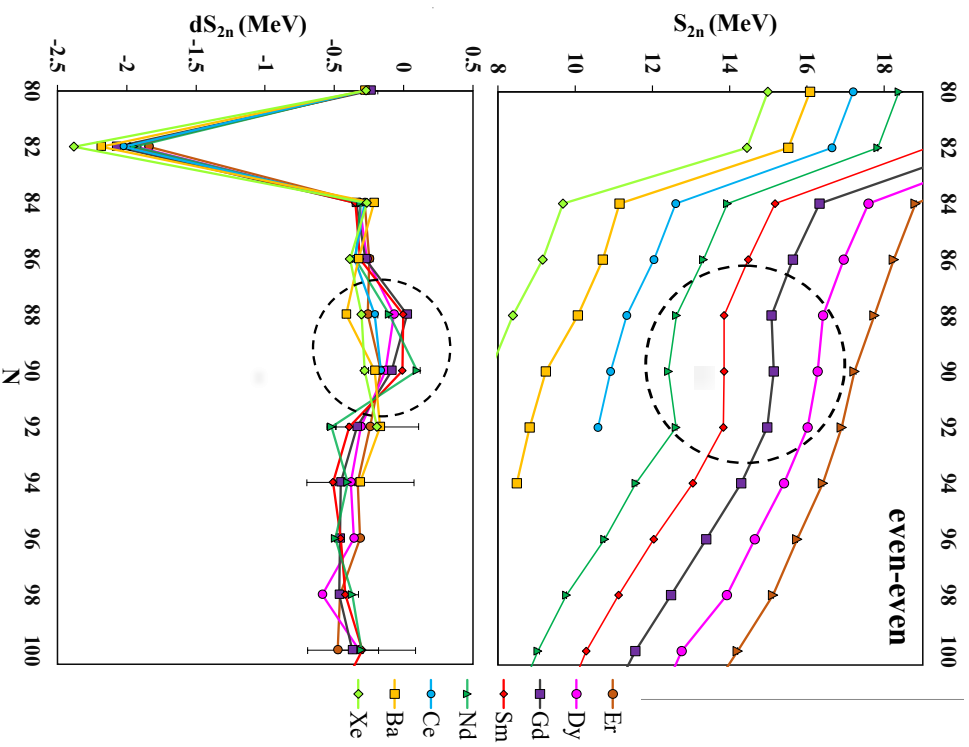


Fig. 4.3 Two-neutron separation energy and its first derivative for proton-even and neutron-even nuclei above the shell closure at $N = 82$. The $N = 90$ shape-phase transition region is indicated with a dashed circle. Extrapolated values are not considered. Data from [38].

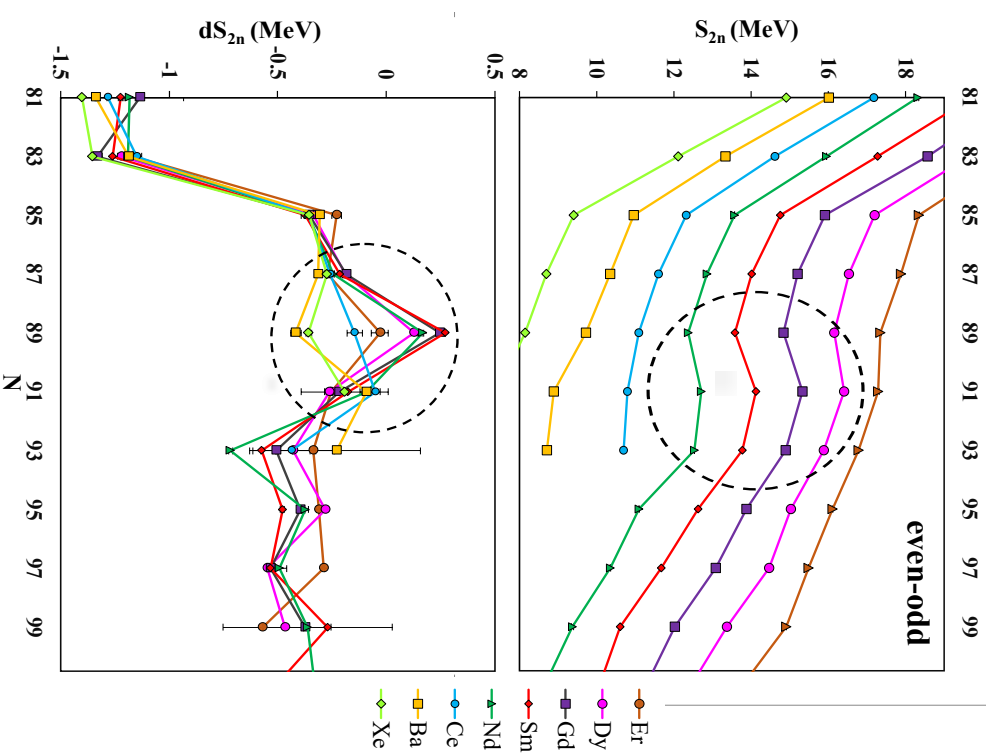


Fig. 4.4 Two-neutron separation energy and its first derivative for proton-even and neutron-odd nuclei above the shell closure at $N = 82$. The $N = 90$ shape-phase transition region is indicated with a dashed circle. Extrapolated values are not considered. Data from [38].

Chapter 5

Data Acquisition systems

The FRS and FRS-IC have two independent particle identification (PID) methods, which have been detailed in Chapter 3. This chapter presents the first time coupling between the FRS and the MR-ToF-MS PID systems at GSI.

5.1 FRS and FRS-IC DAQ coupling

The coupling of both systems allows for standard operation full event-by-event correlation for rates up to a ~ 50 Hz for FRS signals. In order to include the high-resolution mass measurement information from the MR-ToF-MS in the Data AcQuisition System (DAQ) of the FRS, the start and stop signals have been split and recorded simultaneously in both FRS and MR-ToF-MS DAQ systems. Moreover, in the FRS DAQ the events, including the high-resolution mass measurements, have been time-tagged with local time stamps, giving a unique time-label to each event recorded before and after the CSC and therefore making possible a correlation between the two setups. A schematic view of the electronic ensemble used for the coupling of the two DAQ systems is shown in Fig. 5.1.

5.2 Measurement calibration and accuracy

For the experiment discussed here, ^{124}Xe ions at an energy of 600 MeV/u have been impinged on a 1622 mg/cm^2 beryllium target in the interaction area at the entrance of the FRS. The primary beam spills were 5 s long with a 10 s pause interval in between. The IoI used to test the coupling of the systems was ^{109}In .

The mass spectrum measured with the MR-ToF-MS covers a very large mass range of 30 mass units. However, even with a large mass window it was possible to resolve both the ground state of the IoI and the two isomeric states as shown in Fig. 5.2.

Shown in Fig. 5.2 are Gaussian fits of the three nuclear states as well as their evaluated values [43] (dotted lines). The relative mass difference between literature [43] and measurement $(m_{\text{measured}} - m_{\text{literature}})/m_{\text{literature}}$ obtained in the case of ground state and second isomeric state is of the order of 10^{-7} , while for the first isomeric state, it is large as the simple Gaussian peak shape applied here is not sufficient to handle the overlapping peaks [44].

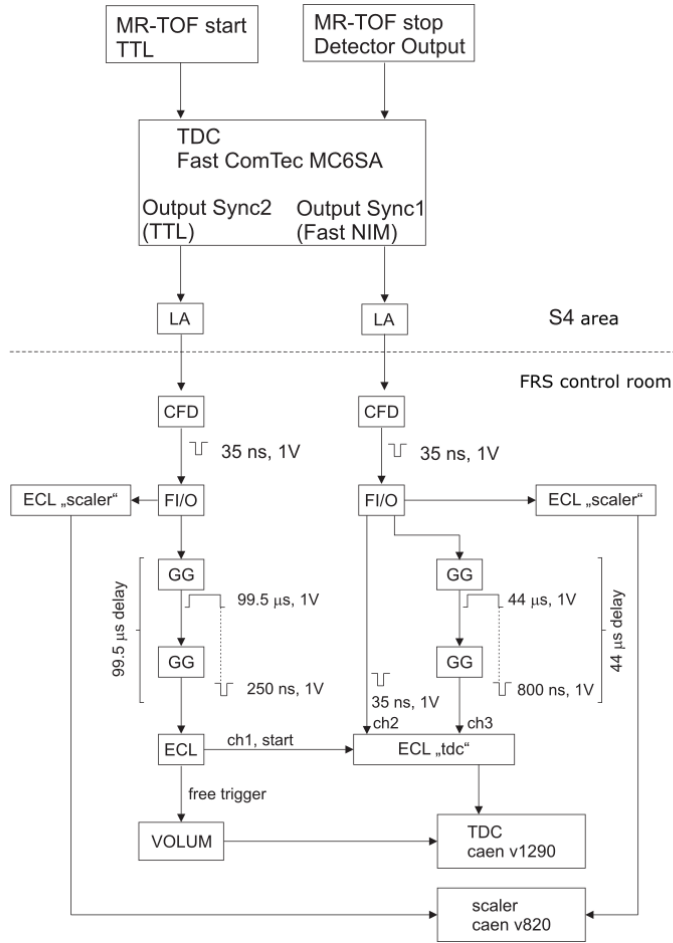


Fig. 5.1 Electronic scheme used for the coupling of the two DAQ systems. Figure from Ref. [39].

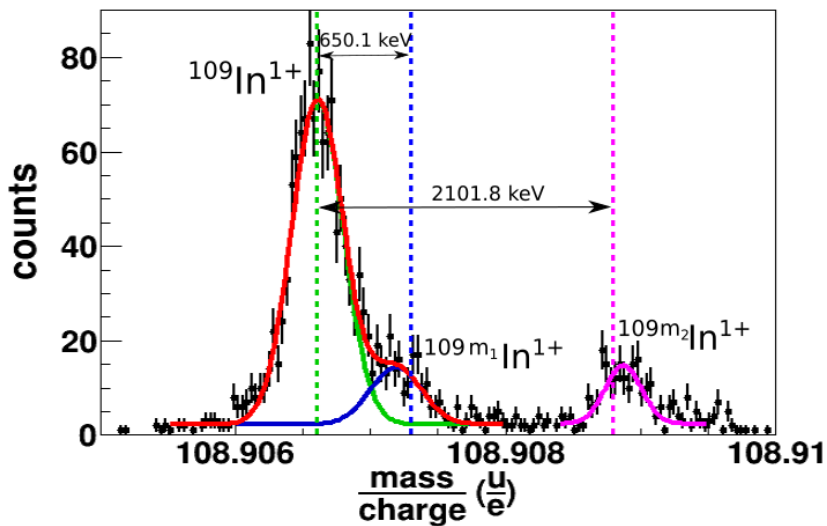


Fig. 5.2 Measured mass-to-charge spectrum of $^{109}\text{In}^{1+}$ ground state and two isomeric states that has been recorded after signal splitting with the FRS Data Acquisition System. The literature mass values [40, 41] of the ground and isomeric states are shown with dotted lines. Figure from Ref. [42].

5.3 Improved signal-to-noise ratio based on spill structure

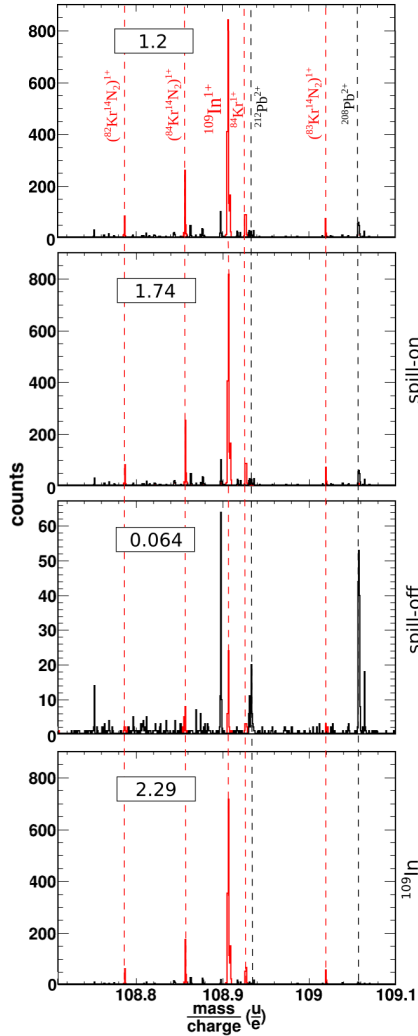


Fig. 5.3 Comparison between full measured mass-to-charge spectrum (upper panel), measured mass-to-charge spectrum when spill-on cut is applied (second panel), mass-to-charge spectrum when spill-off cut is applied (third panel) and mass-to-charge spectrum when a gate on $^{109}\text{In}^{1+}$ in the PID plot was applied (bottom panel). Dashed lines indicate ions that have been significantly suppressed. Figure from Ref. [42].

In Fig. 5.3 is presented the comparison between the full recorded mass spectrum (top panel), the one recorded during the time of the spills (second panel) and the one recorded during the time interval between the spills (third panel). An evaluation of the procedure was performed by looking to the signal ($^{109}\text{In}^{1+}$ counts) to background (counts, which do not belong to the IoI, ions from the calibration source or to a Kr isotope). With this method an increase of more than 50% in the signal-to-background ratio can be achieved, having 98% efficiency ($^{109}\text{In}^{1+}$ counts with versus without cut). Moreover, as expected, a suppression of calibration ions was observed and indicated in Fig. 5.3.

5.4 On-line monitoring

The correlation of the FRS and the MR-ToF-MS PID opens the possibility for real time measurement of some crucial parameters relating to the operation of the FRS and the FRS-IC facilities, such as the CSC extraction time. This makes possible the real time observation of space charge effects in the CSC or of the device drifting from optimal parameters.

The comparison of the time distributions of all ions detected before CSC (black) and $^{109}\text{In}^{1+}$ ions detected in the MR-ToF-MS (blue), shown in Fig. 5.4, evidences a time shift. It represents the sum of the extraction time of the CSC and the time until the ions reach the detector at the end of the MR-ToF-MS. The extraction time evaluation is given by the shift of the distribution of ions before the CSC, shown in red in Fig. 5.4. A difference of 120 ms between the distributions is observed.

5.5 Improved signal-to-noise ratio by event correlation

As time information was proven to be effective in suppressing a part of the background, it can also be used in performing a detailed event-by-event correlation between ions in front of and behind the CSC.

To validate this procedure, all $^{109}\text{In}^{1+}$ ions identified with the FRS PID (detailed in Section 3.4.1) have been selected, as it is indicated in Fig. 5.5. The time interval necessary for the extraction and detection is assumed to be between 40 and 200 ms, and is imposed as a time window following the FRS PID event. Ions detected by the MR-ToF-MS within this window have been added to the histogram presented in Fig. 5.3 (bottom panel). 90% of the total $^{109}\text{In}^{1+}$ ions measured with MR-ToF-MS fall within the time window. Due to the high rates during a spill, a gate on a different isotope (e.g. $^{112}\text{Sn}^{1+}$) in the PID plot leads to a precise description of the spill on time and with this to an increase to 2.37 in the rate of detected $^{109}\text{In}^{1+}$ ions to all counts, which do not belong to the IoI or to a Kr isotope.

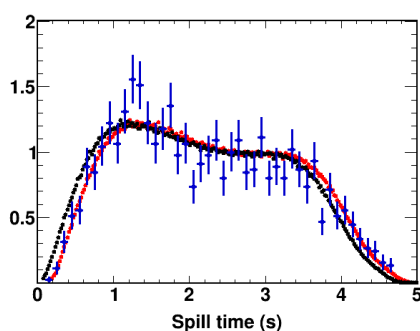


Fig. 5.4 Comparison between spill time distribution of all ions passing the scintillation detector before CSC (black points) and $^{109}\text{In}^{1+}$ ions measured with MR-ToF-MS (blue points). The time difference between the black and the red points is 120 ms, this difference reflects the difference between stopping of the ions in the CSC and their detection in the MR-ToF-MS (see explanation in the text). Figure from Ref. [42].

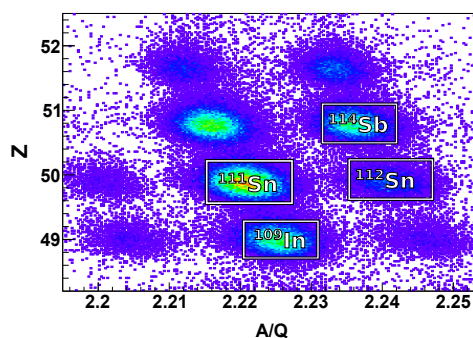


Fig. 5.5 White boxes give the selection of ions in FRS PID plot which are further used in checking the ions to be detected as singly charged with MR-ToF-MS. Figure from Ref. [42].

5.6 Summary

The method presented is a first step in extending the FRS PID with additional information which improves the experimental results with a more precise identification of the IoI.

The work presented in this Chapter is included in the following publications: A. Spătaru, *Extension of the particle identification at the GSI Fragment Separator by high resolution mass spectrometry*, 2016, Master Thesis, Faculty of Physics, University of Bucharest, A. Spătaru et al., *First coupling of the FRS particle identification and the FRS-Ion Catcher data acquisition systems: The case of ^{109}In* , Nucl. Instr. and Meth. in Phys. Res. B 522, 2022.

Chapter 6

Fission fragment measurements and mass evaluation at the FRS-IC

Spontaneous fission, discussed in details in Chapter 2, is an accessible reaction mechanism for the production of neutron-rich nuclei, since it does not require any external interaction. This chapter discusses the mass measurements of spontaneous fission products performed at the FRS-IC setup.

6.1 Experimental setup and measurements

A ^{252}Cf source of 37 kBq activity was mounted inside the CSC and the ToF of the spontaneous fission products were measured with the MR-ToF-MS. A total of five experimental runs took place, from which four were set to undergo a high number of turns (320 and 350) in the analyzer while in one run the turn number was lower (64). A total of 68 different ions, situated north-east to the magic numbers $Z = 50$ and $N = 82$, were extracted from the CSC as doubly-charged.

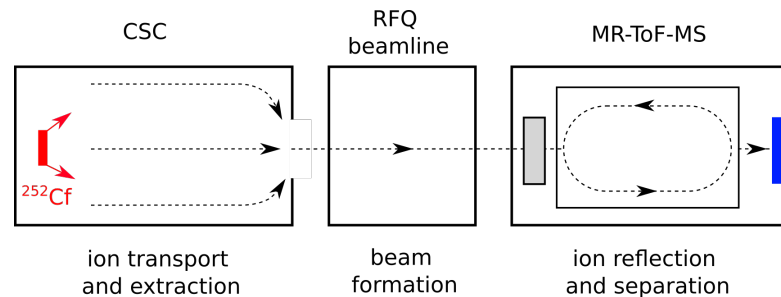


Fig. 6.1 Schematic representation of the FRS-IC setup used in the discussed measurements. The ^{252}Cf source, shown in red, was placed inside the CSC. The IoI are transported and extracted from the CSC and send to the MR-ToF-MS by the RFQ beamline. There an injection trap, shown in gray, is storing the ions before they undergo several reflections inside an analyzer. In blue is the ToF detector at the end of the MR-ToF-MS. Figure from Ref.[45].

6.2 Data evaluation procedure

The mass evaluation of the ToF measurements is an elaborated procedure developed by the FRS-IC group and detailed in Ref. [44].

6.2.1 Conversion to mass spectrum and calibration

The MR-ToF-MS provides ToF measurements which are converted to mass-to-charge, m/q , using Eq. 6.1. Here, Δt , the time ions are stored in the MR-ToF-MS, and N_{it} , the number of turns ions undergo inside the mass analyzer, are two known measurement parameters. The parameters c and b are linked to the length of one turn, s_{turn} , the length from trap to detector without turns, s_0 , and the average electric potential in the analyzer, U , by $b = \frac{s_{turn}}{s_0}$, $c = \frac{2eU}{s_0}$. The last parameter of the formula, t_0 , is a delay coming from electronics.

$$\frac{m}{q} = c \frac{(\Delta t - t_0)^2}{(1 + N_{it}b)^2} \quad (6.1)$$

During the measurement, the voltages applied to the analyzer electrodes can drift causing that the ions with the same mass-to-charge undergo different path lengths and therefore the measured peak broadens. This effect is influencing the parameter b . Its correction implies a calculation of the trend of the parameter over the full time interval, usually referred to as a time resolved calibration (TRC). The impact of the voltages drift on a measurement of few hours and the effect of the TRC is illustrated in Fig. 6.2.

The influence of the calibrants on parameter c was tested by removing one ion species at a time from the calibrants. In Fig. 6.3 is shown the behavior of parameter c over the corresponding turn number of the ion subtracted. This study indicates that the variation of parameter c to its mean is small independent on the ion which is subtracted. Consequently, the calibrant ions can be treated as IoIs as well.

6.2.2 Determination of the peak shape

In ToF spectrometry, for a given spectrum, the peak shape of an ion is independent on the ion's species. This allows the determination of the peak shape from a high abundant peak and use it for the mass calculation of the IoIs.

The parameters of the peak shape are obtained using a hyper-Exponentially Modified Gaussian (hyper-EMG) [20] with a Least-Square fit. The hyper-EMG function, Eq. 6.2. Here, A represents the area of the peak and σ_G and μ_G the Gaussian mean and standard deviation. The scale and strength of the positive and negative exponential distribution are represented by τ and η and their relative strength to one of the positive or negative orientations by Θ .

$$f(x) = A\Theta \sum_{i=1}^m \frac{\eta_{-i}}{2\tau_{-i}} \exp \left[\left(\frac{\sigma_G}{\sqrt{2}\tau_{-i}} \right)^2 + \frac{(x - \mu_G)}{\tau_{-i}} \right] \operatorname{erfc} \left[\frac{\sigma_G}{\sqrt{2}\tau_{-i}} + \frac{(x - \mu_G)}{\sqrt{2}\sigma_G} \right] \\ + A(1 - \Theta) \sum_{i=1}^m \frac{\eta_{+i}}{2\tau_{+i}} \exp \left[\left(\frac{\sigma_G}{\sqrt{2}\tau_{+i}} \right)^2 - \frac{(x - \mu_G)}{\tau_{+i}} \right] \operatorname{erfc} \left[\frac{\sigma_G}{\sqrt{2}\tau_{+i}} - \frac{(x - \mu_G)}{\sqrt{2}\sigma_G} \right] \quad (6.2)$$

In Fig. 6.4 is shown the fit of ^{142}Ba using the hyper-EMG function.

When performing the fit of the IoI, the parameter μ is free, while Θ and η are taken from the peak shape determination. Parameters σ and τ are scaled to the IoI as in Eq. 6.3 where $R_{calibrant}$ and R_{IoI} represent the resolving power of the calibrant ion used for the peak shape determination

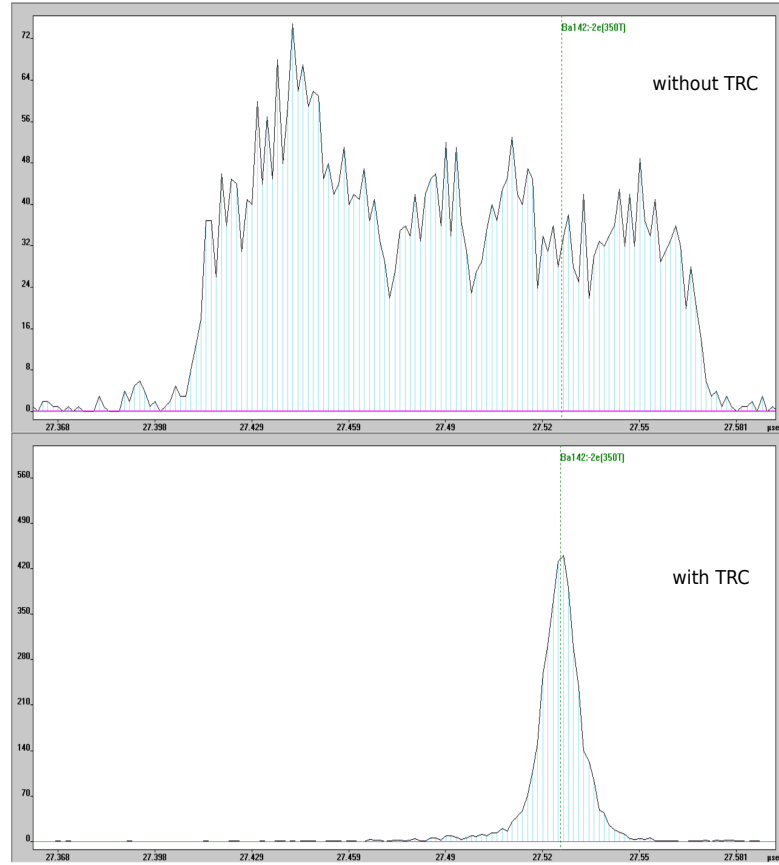


Fig. 6.2 Spectra of the ^{142}Ba as seen with the MAc software without performing a TRC (upper panel) and after (bottom panel).

and the one of the IoI.

$$S = \frac{R_{\text{calibrant}} \cdot \left(\frac{m}{q}\right)_{\text{IoI}}}{R_{\text{IoI}} \cdot \left(\frac{m}{q}\right)_{\text{calibrant}}} \quad (6.3)$$

6.2.3 Mass and uncertainty determination

The method used in the case of overlapping unresolved peaks follows the one mentioned in AME20 [38]. In this case the measured mass-to-charge is calculated as the average between the ground state and isomeric state mass values, Eq. 6.4.

$$\overline{\left(\frac{m}{q}\right)} = \frac{1}{2} \left[\left(\frac{m}{q}\right)_{\text{ground-state}} + \left(\frac{m}{q}\right)_{\text{isomer}} \right] \quad (6.4)$$

The total uncertainty of each measured IoI, σ_{total} , is calculated as the quadratic sum of several uncertainty contributions, Eq. 6.5. In the case of the fission fragments measurements, eight uncertainty contributions were considered and are further detailed.

$$\sigma_{\text{total}} = \left(\sum_i \sigma_i \right)^{1/2} \quad (6.5)$$

1. Statistical uncertainty ($\sigma_{\text{Statistical}}$) is determined using an empirical approach.

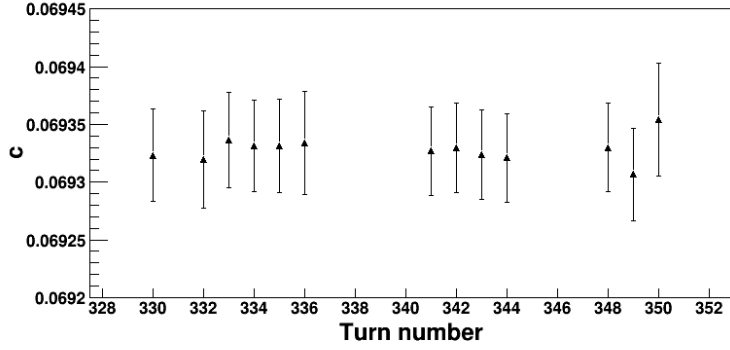


Fig. 6.3 Dependence of the parameter c over the turn numbers of the calibrants used in one of the measurements.

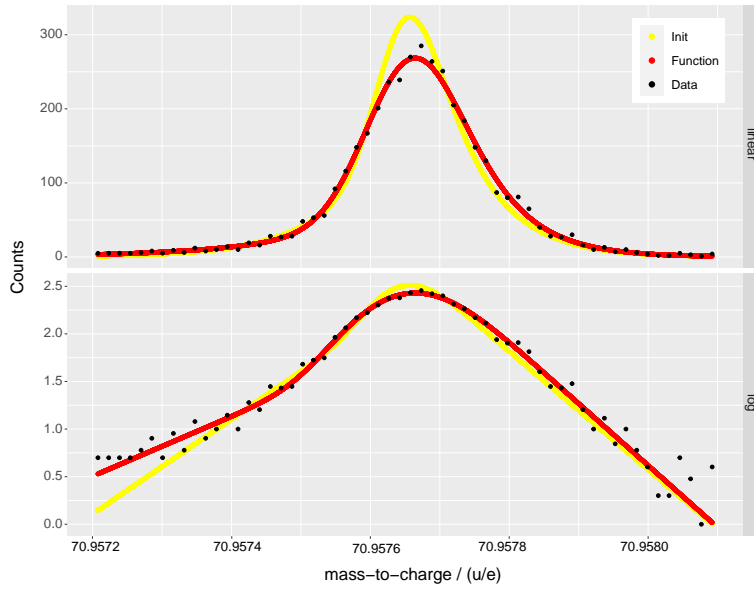


Fig. 6.4 Fit of ^{142}Ba with the Least Square (LS) method using the Hyper-EMG function of Eq.6.2 (red), shown with linear scale (top) and logarithmic scale (bottom). With yellow line is the initial estimation and with black point are represented the data.

2. Calibration parameters (t_0, c) uncertainties (σ_{t_0}, σ_c): Parameters t_0 and c from Eq. 6.1 are determined together with their uncertainties using the MAc software, see Section 6.2.1.
3. Calibrant ion uncertainty ($\sigma_{\text{Calibrant}}$): It is calculated using Eq. 6.6, where the $\sigma_{(m/q)_{lit}}$ and $\sigma_{(m/q)_{fit}}$ denote the literature uncertainty and the statistical uncertainty of the fitted calibrant.

$$\sigma_{\text{calibrant}} = \left(\frac{m}{q}\right)_{\text{IoI}} \cdot \sqrt{\left(\frac{\sigma_{(m/q)_{lit}}}{\left(\frac{m}{q}\right)_{lit}}\right)^2 + \left(\frac{\sigma_{(m/q)_{fit}}}{\left(\frac{m}{q}\right)_{fit}}\right)^2} \quad (6.6)$$

4. Peak shape uncertainty ($\sigma_{\text{peak-shape}}$): The mass uncertainty contribution is coming from the parameters of the peak shape fit and from the influence of the TRC on the peak broadening.

5. Contamination and Background uncertainties ($\sigma_{Contamination}$, $\sigma_{Background}$): Are determined based on the density and average area of the contamination peaks, which are calculated with MAc software.
6. Non-Ideal Ejection (NIE) uncertainty (σ_{NIE}): The calculation of the NIE uncertainty follows an empirical approach by using measurements of the ToF deviation (Δt_{NIE}) during a scan of the time ions are stored inside the analyzer. This measurement is performed for a reference ion of mass-to-charge $\left(\frac{m}{q}\right)_{ref}$. The NIE uncertainty of the IoI is calculated using Eq. 6.7 [44], where $t_{total,IoI}$ represents the total ToF of the IoI and $\left(\frac{m}{q}\right)_{IoI}$ its measured mass-to-charge.

$$\sigma_{NIE} = \frac{2\Delta t_{NIE}}{t_{total,IoI}} \sqrt{\left(\frac{m}{q}\right)_{IoI} \left(\frac{m}{q}\right)_{ref}} \quad (6.7)$$

7. Isomeric contamination uncertainty (σ_{isomer}): The calculation of the mass uncertainty due to the contamination of the IoI with unresolved isomeric state follows the method discussed in AME20 [38], Eq. 6.8.

$$\sigma_{isomer} = \frac{\sqrt{3}}{6} \left[\left(\frac{m}{q}\right)_{isomer} - \left(\frac{m}{q}\right)_{ground-state} \right] \quad (6.8)$$

6.2.4 Averaging method for several independent measurements

In many cases, several independent measurements are available for the same isotope. Therefore an averaging method is needed to calculate a final mass and uncertainty value.

The averaging procedure applied to the analysis of the data at the FRS-IC uses the weighted mean method in which all measured masses of a given isotope (their number is denoted further by K) are weighted inversely proportional to the square of their total uncertainty, $\frac{1}{\sigma_{total,j}^2}$, Eq.6.9.

$$\bar{m}_{eval} = \frac{\sum_{j=1}^K \frac{m_j}{\sigma_{total,j}^2}}{\sum_{j=1}^K \frac{1}{\sigma_{total,j}^2}} \quad (6.9)$$

The averaging of the uncertainties implies the division of the individual uncertainties into two categories: dependent and independent on the experimental conditions. The two groups are quadratically added to generate the total uncertainty of each IoI, Eq. 6.10. The total independent and dependent uncertainties of each ion are calculated by using the variance of the weighted mean (independent part) and the weighted mean (dependent part), Eq. 6.11.

$$\sigma_{total,\bar{m}}^2 = \sigma_{independent,\bar{m}}^2 + \sigma_{dependent,\bar{m}}^2 \quad (6.10)$$

$$\sigma_{total,\bar{m}}^2 = \frac{\sum_{i=1}^N \frac{\sigma_{indep,i}^2}{\sigma_{total,i}^4} + \left(\sum_{i=1}^N \frac{\sigma_{dep,i}}{\sigma_{total,i}^2} \right)^2}{\left(\sum_{i=1}^N \frac{1}{\sigma_{total,i}^2} \right)^2} \quad (6.11)$$

As a result of this method, the contribution of the indirect uncertainties is reduced, while the dependent part stays unchanged. An example of the effects of the averaging procedure is shown in Fig. 6.5 for ^{157}Sm .

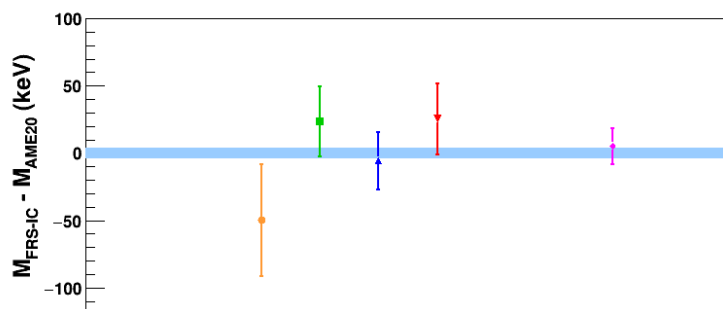


Fig. 6.5 Mass deviation to the AME20 value of four independent measurements of ^{157}Sm from four high-turn runs (orange, green, blue and red) compared with the calculated average value (purple). The blue shaded area in the figure provides the AME20 uncertainty.

6.2.5 Fission fragments calibration results

In Fig. 6.6 is shown the mass deviation distribution over the turn numbers for one of the high turn number measurements. The results show a well agreement through a scattering around zero. This result offers the possibility of performing a re-calibration using the same ion for all IoIs in the spectrum.

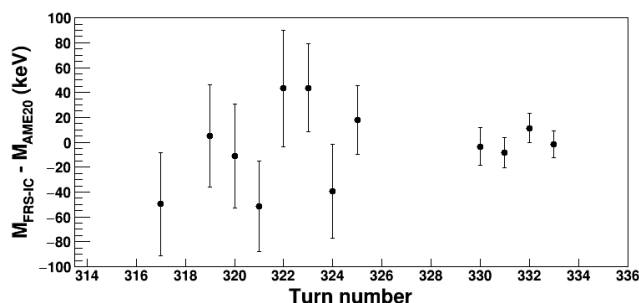


Fig. 6.6 Mass deviation to AME20 values of the calibrants used in one of the high turn number measurements. On the x-axis is shown the turn number that the corresponding calibrant underwent in the analyzer.

6.3 Summary

This chapter presented the mass measurements of neutron-rich nuclei performed at the FRS-IC together with the data evaluation procedure followed in order to get accurate mass values.

The data evaluation discussed in this chapter will be included in a forthcoming publication: A. Spătaru et al., *Accurate mass measurements near the $N=90$ shape phase transition region at the FRS-IC*, in progress

Chapter 7

Mass measurements and shape-phase transition at $N = 90$

The experimental program performed at the FRS-IC for measurements of ^{252}Cf spontaneous fission products and their mass evaluation procedure were discussed in detail in Chapter 6. The connection between the ground state masses and the phase transition through the evolution of the S_{2n} and dS_{2n} parameters was presented in Chapter 4.

In this chapter the mass results are presented and compared with their previous direct or indirect measurements. Their overlap with the $N = 90$ shape phase transition region allows for investigations of the change between the nuclear shapes using direct mass measurements. S_{2n} and dS_{2n} values are calculated using the measured masses and the deviations from linearity in their evolution over the neutron number are discussed.

7.1 Experimental results

Almost 70 masses were measured simultaneously in an experimental campaign that took place at the FRS-IC setup. A big part of them have been previously measured at Penning trap facilities such as CARIBU and JYFLTRAP. A third of the masses don't have a previous direct measurement, their masses being calculated from measurements of the energy released in a nuclear reaction or decay. In this section, the measurements are compared with their previous values.

7.2 Discussion

The measured masses were used to calculate the S_{2n} and dS_{2n} values of the corresponding nuclei. Their evolution over the neutron number is studied for nuclei separated based on the evenness or oddness of the protons and neutrons. The trend is compared to the one of theoretical calculations of a model based on a Hartree-Fock approach.

7.3 Summary

The measurements of nuclei at $N = 90$ demonstrates the capabilities of the FRS-IC setup for direct mass measurements of spontaneous fission products.

The values of the S_{2n} and dS_{2n} calculated with the FRS-IC measurements confirm the deviations from the linear decrease and respectively the peaks for the well-known Nd and Sm nuclei. The values for the Ce nuclei have been compared with a theoretical model and show a perfect agreement in the even-even case.

The measurements and discussion in this chapter are included in the following publications: A. Spătaru et al., *Nuclear Structure Studies with High-Precision Mass Measurements of Spontaneous Fission Fragments at the FRS Ion Catcher*, Bulg. J. Phys. 48, 535-540 (2021); A. Spătaru et al., *Accurate mass measurements near the $N=90$ shape phase transition region at the FRS-IC*, in progress

Chapter 8

Heavy Neutron-Rich Isotope Production via Multi-Nucleon Transfer Reactions

The MNT process is one of the production mechanisms for neutron-rich nuclei, discussed in Chapter 3, that has shown an increased cross-section for $N = 126$ compared to fragmentation reactions.

This chapter presents the simulated results of exotic neutron-rich production using the MNT reactions for the case of two experimental programs that are planned at the Ion Guide Isotope Separator On-Line (IGISOL) facility at JYFL Accelerator Laboratory and at FRS Ion Catcher at GSI.

8.1 Experimental programs at the FRS-IC and IGISOL

An experimental program to utilize MNT reactions for production of neutron-rich nuclei using the gas-cell technique is planned at the FRS-IC facility. For this purpose, the FRS will be used for beam transport, while the reaction will take place inside the CSC. The planned MNT reactions involve the use of a ^{238}U beam (10^7 particles/s) and four types of targets. Two of the targets, ^{64}Ni and ^{209}Bi , have been studied before in [8] and [46] and will be used for tuning and proof-of-principle measurements. The ^{164}Dy and ^{198}Pt targets will be used in production and measurements of IoIs. In the studies presented in this chapter, only three of the targets are considered: ^{64}Ni , ^{209}Bi and ^{164}Dy . The expectations for ^{198}Pt case will be extrapolated from the studied cases.

Another experimental program that considers the MNT reaction using the gas-cell technique was planned at the IGISOL facility at JYFL. AT the IGISOL facility, the studies are planned to be performed using a ^{136}Xe beam and a ^{209}Bi and a ^{198}Pt target. The $^{136}\text{Xe} + ^{209}\text{Bi}$ program took place and was used to validate the experiment. The results of this experiment are reported in [46].

The emission angles (according to the Langevin-type model [6, 7]) for the reactions planned to be used at both setups, shown in Fig. 8.2, present large cross sections at high angles. A beam dump, which will block the primary beam from going further into gas, is planned for both experimental programs.

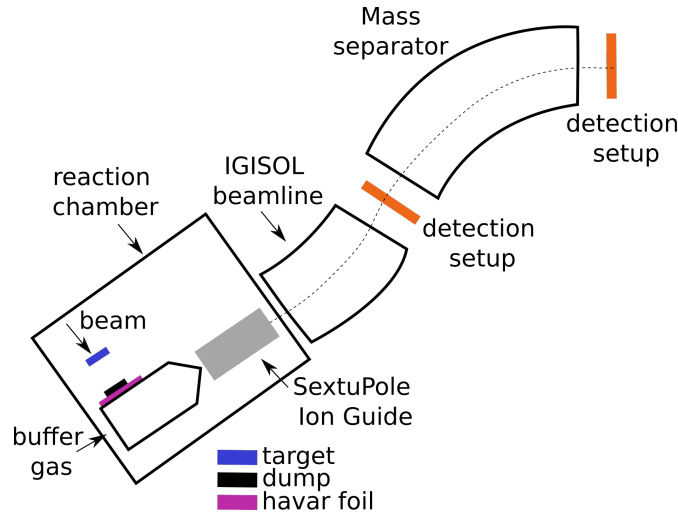


Fig. 8.1 Schematic drawing of the MNT setup configuration at the IGISOL facility at JYFL. Figure from [47].

The two setups are limited in their energy and angular acceptance. Hence, a precise optimization

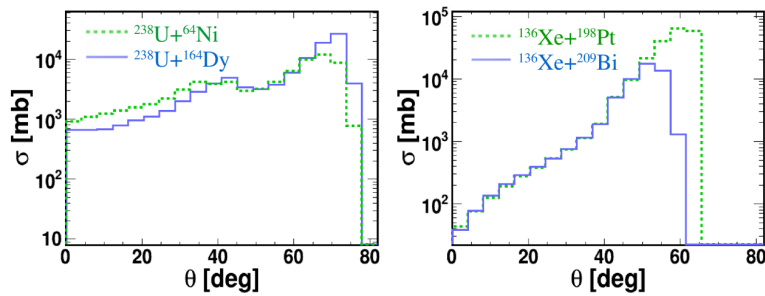


Fig. 8.2 Reaction cross sections for TLFs, calculated within the Langevin-type model, as a function of the emission angle for the reactions considered for experiments at the two setups: FRS-IC (left panel) with ^{238}U beam at 2856 MeV on ^{64}Ni and ^{164}Dy , and IGISOL (right panel) with ^{136}Xe at 890 MeV on ^{209}Bi and at 885 MeV on ^{198}Pt . Figure from [48].

of the experiment is crucial in order to maximize the yields.

8.2 Process and setup implementation in GEANT4

Simulations starting with the generation of the reaction products in target up to their thermalization in the buffer gas of the cell have been performed with the GEANT4 simulation toolkit and analyzed with ROOT. The purpose of the simulations with the FRS-IC setup was to optimize the target thickness and CSC length in order to maximize the generation and thermalization of the reaction products, as well as to study the rates of the IoIs. On the other hand, the simulations with the IGISOL setup were used for the comparison with the measurements. For these studies, three modules were added to the software:

1. **Primary beam generation:** Here the properties of the primary beam are described.
2. **Reaction cross-sections:** Here are implemented the reactions cross sections which are calculated with GRAZING and Langevin-type model using Eq. 8.1 and 8.2.

$$\sigma_{\text{Grazing}}(E/A) = \frac{\sigma(E, A, Z)}{\sum_{A, Z} \sigma(E, A, Z)} \quad (8.1)$$

$$\frac{d^4 \sigma_{\text{Langevin}}}{dZ dA dE d\Omega}(A, Z, E, \theta) = \int_0^{b_{\text{max}}} \frac{\Delta N(b, A, Z, E, \theta)}{N_{\text{tot}}(b)} \frac{bdb}{\Delta Z \Delta A \Delta E \sin \theta \Delta \theta} \quad (8.2)$$

3. **Geometry of the experimental setup:** The geometries of the IGISOL and FRS-IC setups are implemented as it is shown schematically in Fig. 8.3.

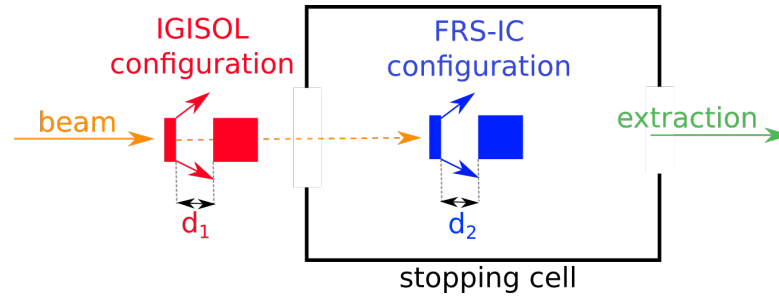


Fig. 8.3 Schematic representation of the experimental setups implemented in GEANT4 for both IGISOL and FRS-IC configurations. The distances between target and dump are denoted by d_1 and d_2 and with arrows are indicated the products released from the target. Figure from [48].

8.3 Simulation with the FRS-IC setup

8.3.1 Results using GRAZING model

The first step of the simulation is finding the optimal thickness of the ^{64}Ni target for which the maximum rate of reaction products is released in the gas of CSC. The generated and released product rates, as function of the target thickness, are shown in Fig. 8.4 with red circles and blue squares, respectively. The optimal target thickness is of $40 \mu\text{m}$.

A beam dump with a thickness of 3 mm and the same diameter as the target is placed 5 cm after the target and inside the gas cell.

The dependence of the stopped product rate on the length L of the gas cell is shown in Fig. 8.5. While a saturation rate is reached for lengths around 60 cm, taking into account the optimal value of 25 cm for space charge and ion drift effects discussed above implies that the optimal CSC length is around 40 cm.

The distributions of the generated (black circles) and released (red circles) ions/s as a function of the energy is shown in Fig. 8.6. In summary, for a CSC length of 40 cm, about 3.8% of the PLF and the TLF are stopped in the gas of the CSC, resulting in the rates of stopped reaction products of approximately 47 PLFs/s and 6 TLFs/s.

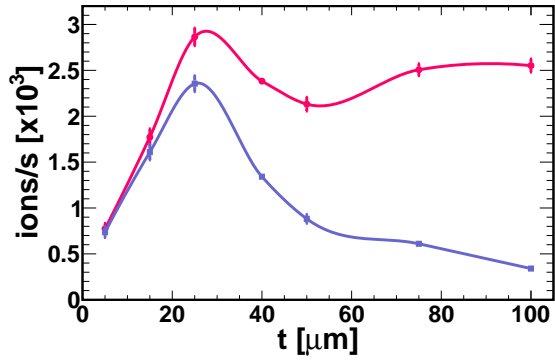


Fig. 8.4 Rate of generated ions (red) compared to rate of released ions (blue) as function of the thickness of the target. Figure from [48].

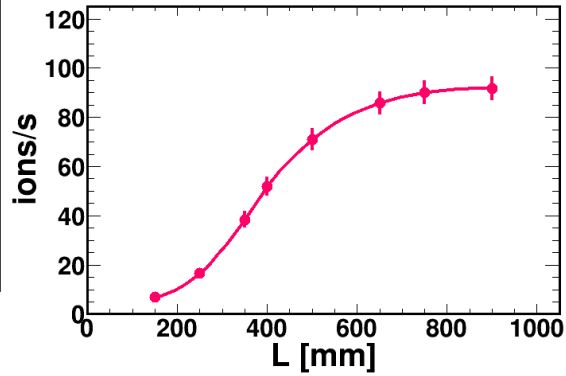


Fig. 8.5 Rate of stopped ions for different lengths of the cell. Figure from [48].

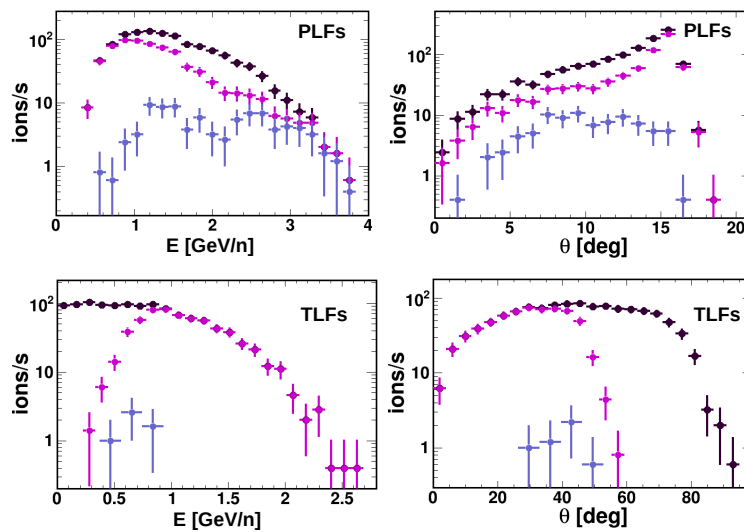


Fig. 8.6 Left top and bottom panels show the PLF and TLF energy distributions. Right top and bottom panels show the PLF and TLF angular distributions. Black, red and blue circles show generated, released and stopped rates, respectively. Figure from [48].

Space charge effect

The primary beam penetrating the target is generating space charge in the region below the beam dump.

The Potential Energy Surface (PES) of the electric field generated by the DC electrodes of the CSC, as calculated by the SIMION 8.1 software, is shown in Fig. 8.7 for the longitudinal plane (left panel) and the transversal plane (right panel).

The effect of the induced space charge on the reaction product trajectories is shown in Fig. 8.8. The Particle-In-Cell (PIC) library of SIMION 8.1 dynamically computes the time and space dependent electric field generated by all heavy ions and He^+ ions, as they propagate and interact among themselves in the applied DC field shown in Fig. 8.7. In conclusion, no significant impact of the primary space charge region on the heavy ion extraction time and efficiency is found in these calculations.

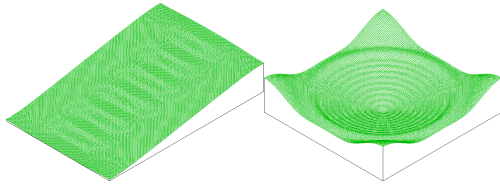


Fig. 8.7 Electric PES of the CSC electrodes: longitudinal component in the left panel and transversal component in the right panel. Figure from Ref. [48].

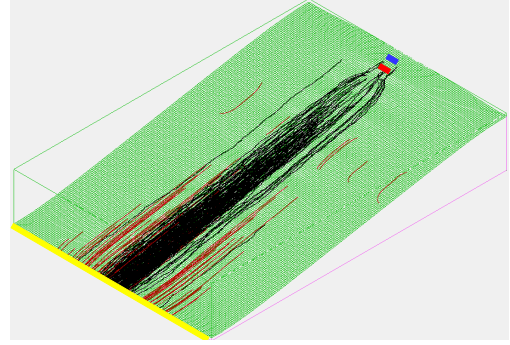


Fig. 8.8 PIC simulation of the heavy (red lines) and He^+ (black lines) ion trajectories in the applied PES (green mesh) with the SIMION 8.1 software. The target is shown as a blue box, the beam dump as a red box and the carpet as a yellow line. Figure from [48].

8.3.2 Results using Langevin-type model

Simulations regarding the MNT reaction at FRS-IC have been performed using reaction cross sections from the Langevin-type model. In this case, three types of targets have been considered: ^{64}Ni , ^{209}Bi and ^{164}Dy . The results include an optimization of the thicknesses of the three targets based on the number of ions/s released from the targets and further thermalized inside the helium gas of the CSC and of their energy and emission angle distributions. The optimization of the length of the CSC is done by studying the rate of ions/s thermalized at different lengths of the cell.

8.4 Measurements and simulations using the IGISOL setup

Measurements of the MNT process using the $^{136}\text{Xe} + ^{209}\text{Bi}$ reaction took place at the IGISOL and were reported in Ref. [46]. The dominant peak of the spectrum is ^{211}Ba , followed by the ground-state and isomeric state of ^{211}Po . Due to the low efficiency of the setup (below 10%) the two states of ^{211}Po were measured with a rate of 45 counts/min.

Simulations of the experiment were done using reaction cross-section estimated with the Langevin-type model, which were implemented in GEANT4 together with the characteristics of the experimental setup.

In Fig. 8.9 are given the energy-angle distributions for TLFs ($204 < A < 214$) and ^{211}Po ions at three positions in the experimental setup. Because most of the IoIs are produced with energies of 1-1.5 MeV/A, they will be released from the havar window into the helium gas with energies of 0.1-0.7 MeV/A and only few ions (< 0.5 ^{211}Po /s) fulfill the conditions for being thermalized.

A second reaction, $^{136}\text{Xe} + ^{198}\text{Pt}$, is planned to be measured using the IGISOL setup. The results of the GEANT4 simulations are shown in Fig. 8.10 for two different thicknesses of the ^{198}Pt target. In the case of the $6\ \mu\text{m}$ target, the TLFs are released at lower E/A than for the $3\ \mu\text{m}$ target because of the increased number of scatterings in the target. This characteristic will allow for a higher number of thermalized ions when the $6\ \mu\text{m}$ target is used.

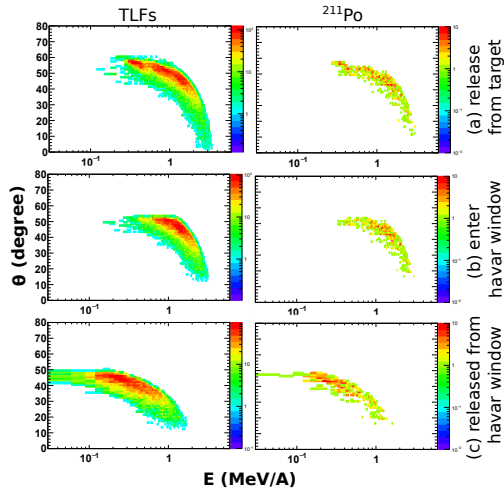


Fig. 8.9 Simulated energy-angle ($E - \theta$) distributions of the TLFs and ^{211}Po from $^{136}\text{Xe} + ^{209}\text{Bi}$ reaction that: (a) are released from the target (b) enter the havar window (c) are released from the havar window for TLFs and ^{211}Po

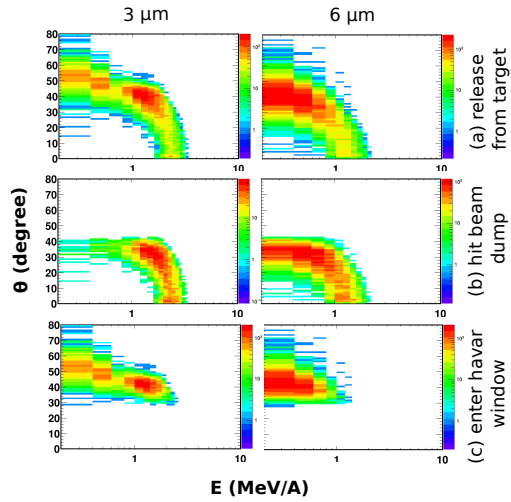


Fig. 8.10 Simulated energy-angle ($E - \theta$) distributions of the TLFs from $^{136}\text{Xe} + ^{198}\text{Pt}$ reaction that: (a) are released from the target, (b) hit beam dump, (c) enter havar window, considering a $3 \mu\text{m}$ and $6 \mu\text{m}$ thick target

8.5 Summary

The study of the MNT reaction using the FRS-IC setup aimed its optimization using both the GRAZING and Langevin-type models and Geant4 simulations. The MNT simulation for the IGISOL setup show a low rate of thermalized ions because of the high energy of the IoIs and the small volume of the gas cell.

The work presented in this Chapter is part of the following publications: A. Spătaru et al., *Production of exotic nuclei via MNT reactions using gas cells*, Acta Physica Polonica B 51, (2020), A. Spătaru et al., *Multi-Nucleon Transfer reactions in $^{238}\text{U} + ^{64}\text{Ni}$ using Grazing model*, U.P.B. Sci. Bull. A 82 (2020), A. Spătaru et al., *Study of exotic nuclei produced in multinucleon transfer reactions at the IGISOL facility*, ELI-NP Annual Reports 2022, A. Spătaru et al., *Multi-Nucleon Transfer studies of ^{238}U induced reactions on ^{64}Ni , ^{164}Dy and ^{209}Bi targets using a Langevin-type model*, in progress

Chapter 9

Summary and Outlook

The Fragment Separator (FRS) [26] and FRS-Ion Catcher (FRS-IC) [27] setups at GSI, Darmstadt were used to perform the measurements discussed in this thesis. The two setups are separated in terms of their data acquisition systems but nonetheless work together in the study of isotopic beams produced via fragmentation reaction.

As a first step, a study regarding the extension of the FRS DAQ system with highly accurate mass information from FRS-IC was performed and included in Ref. [42]. This method has proven the real time measurement of crucial parameters of the FRS-IC setup.

The measurements of spontaneous fission fragments using a ^{252}Cf at the FRS-IC, discussed in Chapters 6, 7 and included in Ref. [45, 49], showed the capabilities of the setup for direct mass measurements of almost 70 ions during one measurement. The measured masses were used to calculate the S_{2n} values and their first derivative (dS_{2n}) of the identified ions, which are known to show deviations from linearity when are examined over the increased neutron number. The measured values confirm the deviations, which is also seen in the calculated values based on a Skyrme-Hartree-Fock-BCS [50] approach.

The current studies can be extended to heavier neutron-rich systems when using nuclear reactions. A mechanism which has recently shown to produce neutron-rich nuclei with high cross sections [1] than the fragmentation reaction is the Multinucleon-Transfer reaction. Two experimental programs planned to take place at the Ion Guide Isotope Separator On-Line (IGISOL) facility at JYFL Accelerator Laboratory and at the FRS IC were studied.

The investigations presented in this thesis are offering crucial information about the behavior of thermalized ions and the measurement of their masses for studies of nuclear structure. Such knowledge is useful for future facilities such as ELISOL setup at ELI-NP. Here, nuclear structure studies of photofission fragments are planned using a gas cell and mass spectrometer [51].

List of figures

2.1	Schematic representation of the fragmentation reaction mechanism from a point of view of the abrasion-ablation model.	2
2.2	Photofission reaction uses photons to excite nuclei to precise energies above the fission barrier.	3
2.3	Abrasion-fission is the process in which at small impact parameters a nucleus abrades after the interaction with a light target. As a consequence the nucleus is left excited and undergoes fission.	3
2.4	Coulomb-fission is the process in which a nucleus gets excited and undergoes fission after the exchange of a virtual photon (indicated as $h\nu$ in the cartoon).	3
2.5	During the multinucleon-transfer reactions the projectile and the target nuclei interact without the formation of a compound nucleus and exchange several nucleons, leading to the formation of a Projectile-like-Fragment (PLF) and Target-like-Fragment (TLF).	4
3.1	First region of the stability diagram as function of the Mathieu parameters. Only mass m_2 lies inside the stability borders, shown in pink, and can be transmitted. The apex of the region is at $a = 0.237$ and $q = 0.706$ and is representing the point where the mass filter would transport only one mass.	6
3.2	Schematic representation of the three oscillations (defined in the legend of the figure) which are describing the motion of the ions inside a Penning Trap.	8
3.3	Representation of the linear (upper figure) and multiple reflection (bottom figure) mass spectrometers. The injection plate and the detector are shown in red and green, respectively. With orange are represented the reflecting mirrors used to increase the flight distance.	9
3.4	Schematic drawing of the FRS [26] and FRS-IC [27] setups. The set of SCI [28], TPC [29] and MUSIC [30, 31] detectors provides the FRS PID, also referred to as identification before the CSC, while the MR-ToF-MS provides by a precision mass measurement the identification after the CSC. Above the corresponding energies in the experimental setup are shown. Below the flight times in the different sections are indicated.	10
3.5	Example of an FRS PID plot in which the system was optimized for the measurement of ^{109}In (upper figure). Range distribution at the final focal plane in Al ions in the FRS PID (lower figure). The calculation is based on fits to data [32]. The areal density and the position of the CSC in range is marked with in red.	10

4.1	Schematic representation of the spherical nuclear shape and the two deformed prolate and oblate shapes.	12
4.2	Ratio between the energy of the first 4^+ and 2^+ excited states around the $N = 90$ critical point for nuclei with an even number of protons and neutrons. Data from https://www.nndc.bnl.gov/ensdf/	13
4.3	Two-neutron separation energy and its first derivative for proton-even and neutron-even nuclei above the shell closure at $N = 82$. The $N = 90$ shape-phase transition region is indicated with a dashed circle. Extrapolated values are not considered. Data from [38].	14
4.4	Two-neutron separation energy and its first derivative for proton-even and neutron-odd nuclei above the shell closure at $N = 82$. The $N = 90$ shape-phase transition region is indicated with a dashed circle. Extrapolated values are not considered. Data from [38].	14
5.1	Electronic scheme used for the coupling of the two DAQ systems. Figure from Ref. [39].	16
5.2	Measured mass-to-charge spectrum of $^{109}\text{In}^{1+}$ ground state and two isomeric states that has been recorded after signal splitting with the FRS Data Acquisition System. The literature mass values [40, 41] of the ground and isomeric states are shown with dotted lines. Figure from Ref. [42].	16
5.3	Comparison between full measured mass-to-charge spectrum (upper panel), measured mass-to-charge spectrum when spill-on cut is applied (second panel), mass-to-charge spectrum when spill-off cut is applied (third panel) and mass-to-charge spectrum when a gate on $^{109}\text{In}^{1+}$ in the PID plot was applied (bottom panel). Dashed lines indicate ions that have been significantly suppressed. Figure from Ref. [42].	17
5.4	Comparison between spill time distribution of all ions passing the scintillation detector before CSC (black points) and $^{109}\text{In}^{1+}$ ions measured with MR-ToF-MS (blue points). The time difference between the black and the red points is 120 ms, this difference reflects the difference between stopping of the ions in the CSC and their detection in the MR-ToF-MS (see explanation in the text). Figure from Ref. [42].	18
5.5	White boxes give the selection of ions in FRS PID plot which are further used in checking the ions to be detected as singly charged with MR-ToF-MS. Figure from Ref. [42].	18
6.1	Schematic representation of the FRS-IC setup used in the discussed measurements. The ^{252}Cf source, shown in red, was placed inside the CSC. The IoI are transported and extracted from the CSC and send to the MR-ToF-MS by the RFQ beamline. There an injection trap, shown in gray, is storing the ions before they undergo several reflections inside an analyzer. In blue is the ToF detector at the end of the MR-ToF-MS. Figure from Ref.[45].	19
6.2	Spectra of the ^{142}Ba as seen with the MAc software without performing a TRC (upper panel) and after (bottom panel).	21

6.3	Dependence of the parameter c over the turn numbers of the calibrants used in one of the measurements.	22
6.4	Fit of ^{142}Ba with the Least Square (LS) method using the Hyper-EMG function of Eq.6.2 (red), shown with linear scale (top) and logarithmic scale (bottom). With yellow line is the initial estimation and with black point are represented the data.	22
6.5	Mass deviation to the AME20 value of four independent measurements of ^{157}Sm from four high-turn runs (orange, green, blue and red) compared with the calculated average value (purple). The blue shaded area in the figure provides the AME20 uncertainty.	24
6.6	Mass deviation to AME20 values of the calibrants used in one of the high turn number measurements. On the x-axis is shown the turn number that the corresponding calibrant underwent in the analyzer.	24
8.1	Schematic drawing of the MNT setup configuration at the IGISOL facility at JYFL. Figure from [47].	28
8.2	Reaction cross sections for TLFs, calculated within the Langevin-type model, as a function of the emission angle for the reactions considered for experiments at the two setups: FRS-IC (left panel) with ^{238}U beam at 2856 MeV on ^{64}Ni and ^{164}Dy , and IGISOL (right panel) with ^{136}Xe at 890 MeV on ^{209}Bi and at 885 MeV on ^{198}Pt . Figure from [48].	28
8.3	Schematic representation of the experimental setups implemented in GEANT4 for both IGISOL and FRS-IC configurations. The distances between target and dump are denoted by d_1 and d_2 and with arrows are indicated the products released from the target. Figure from [48].	29
8.4	Rate of generated ions (red) compared to rate of released ions (blue) as function of the thickness of the target. Figure from [48].	30
8.5	Rate of stopped ions for different lengths of the cell. Figure from [48].	30
8.6	Left top and bottom panels show the PLF and TLF energy distributions. Right top and bottom panels show the PLF and TLF angular distributions. Black, red and blue circles show generated, released and stopped rates, respectively. Figure from [48].	30
8.7	Electric PES of the CSC electrodes: longitudinal component in the left panel and transversal component in the right panel. Figure from Ref. [48].	31
8.8	PIC simulation of the heavy (red lines) and He^+ (black lines) ion trajectories in the applied PES (green mesh) with the SIMION 8.1 software. The target is shown as a blue box, the beam dump as a red box and the carpet as a yellow line. Figure from [48].	31
8.9	Simulated energy-angle ($E - \theta$) distributions of the TLFs and ^{211}Po from $^{136}\text{Xe} + ^{209}\text{Bi}$ reaction that: (a) are released from the target (b) enter the havar window (c) are released from the havar window for TLFs and ^{211}Po	32

8.10 Simulated energy-angle ($E - \theta$) distributions of the TLFs from $^{136}\text{Xe} + ^{198}\text{Pt}$ reaction that: (a) are released from the target, (b) hit beam dump, (c) enter havar window, considering a $3\ \mu\text{m}$ and $6\ \mu\text{m}$ thick target	32
--	----

Keywords: FRS-IC, cryogenic stopping cell, mass measurements, shape phase transition, multi-nucleon transfer.

References

- [1] Y. X. Watanabe and et al. Pathway for the production of neutron-rich isotopes around the $n=126$ shell closure. *Physical Review Letters*, 115(17):172503, oct 2015.
- [2] J.-J. Gaimard and K.-H. Schmidt. A reexamination of the abrasion-ablation model for the description of the nuclear fragmentation reaction. *Nuclear Physics A*, 531(3-4):709–745, sep 1991.
- [3] A.S. Goldhaber. Statistical models of fragmentation processes. *Physics Letters B*, 53(4):306–308, dec 1974.
- [4] A.M. Mattera and et al. Nuclear data sheets for $a=252$. *Nuclear Data Sheets*, 172:543–587, feb 2021.
- [5] Aage Winther. Grazing reactions in collisions between heavy nuclei. *Nucl Phys A*, 572(1):191–235, may 1994.
- [6] A. V. Karpov and V. V. Saiko. Modeling near-barrier collisions of heavy ions based on a langevin-type approach. *Phys Rev C*, 96(2):024618, aug 2017.
- [7] V. V. Saiko and A. V. Karpov. Analysis of multinucleon transfer reactions with spherical and statically deformed nuclei using a langevin-type approach. *Phys Rev C*, 99(1):014613, jan 2019.
- [8] L. Corradi and et al. Multinucleon transfer processes in $^{64}\text{Ni} + ^{238}\text{U}$. *Phys Rev C*, 59(1):261–268, jan 1999.
- [9] Florian Greiner and et al. Removal of molecular contamination in low-energy RIBs by the isolation-dissociation-isolation method. *Nuclear Instruments and Methods in Physics Research Section B: Beam Interactions with Materials and Atoms*, 463:324–326, jan 2020.
- [10] Edmond de Hoffmann and Vincent Stroobant. Mass spectrometry: Principles and applications, 3rd edition. *John Wiley and Sons, Inc.*, 2007.
- [11] J. H. Block. Peter h. dawson: Quadrupole mass spectrometry and its application, elsevier scientific publishing company, amsterdam-oxford-new york 1976. 349 seiten, preis: Dfl 129,-, US \$ 49.75. *Berichte der Bunsengesellschaft für physikalische Chemie*, 81(8):777–777, aug 1977.
- [12] D.Sc Norman William McLachlan. Theory and application of mathieu functions. *Clarendon Press*, 1951.
- [13] H.-Jürgen Kluge. Penning trap mass spectrometry of radionuclides. *International Journal of Mass Spectrometry*, 349-350:26–37, sep 2013.
- [14] G. Graeff, H. Kalinowsky, and J. Traut. A direct determination of the proton electron mass ratio. *Zeitschrift für Physik A: Atoms and Nuclei*, 297(1):35–39, mar 1980.
- [15] Alan G. Marshall and et al. Fourier transform ion cyclotron resonance mass spectrometry: A primer. *Mass Spectrometry Reviews*, 17(1):1–35, 1998.

- [16] Y H Zhang and et al. Storage ring mass spectrometry for nuclear structure and astrophysics research. *Physica Scripta*, 91(7):073002, jun 2016.
- [17] H. Wollnik. Principles of time-of-flight mass analyzers. *Nuclear Instruments and Methods in Physics Research Section A: Accelerators, Spectrometers, Detectors and Associated Equipment*, 298(1-3):156–160, dec 1990.
- [18] I. Mardor and et al. Mass measurements of as, se, and br nuclei, and their implication on the proton-neutron interaction strength toward the $n=z$ line. *Physical Review C*, 103(3):034319, mar 2021.
- [19] M. Ranjan and et al. Design, construction and cooling system performance of a prototype cryogenic stopping cell for the super-FRS at FAIR. *Nuclear Instruments and Methods in Physics Research Section A: Accelerators, Spectrometers, Detectors and Associated Equipment*, 770:87–97, jan 2015.
- [20] S. Purushothaman and et al. First experimental results of a cryogenic stopping cell with short-lived, heavy uranium fragments produced at 1000 MeV/u. *EPL (Europhysics Letters)*, 104(4):42001, nov 2013.
- [21] M. P. Reiter. Pilot experiments with relativistic uranium projectile and fission fragments thermalized in a cryogenic gas filled stopping cell. *PhD thesis Justus-Liebig-University of Gießen*, 2015.
- [22] E. Haettner and et al. New high-resolution and high-transmission modes of the FRS for FAIR phase-0 experiments. *Nuclear Instruments and Methods in Physics Research Section B: Beam Interactions with Materials and Atoms*, 463:455–459, jan 2020.
- [23] T. Dickel and et al. A high-performance multiple-reflection time-of-flight mass spectrometer and isobar separator for the research with exotic nuclei. *Nuclear Instruments and Methods in Physics Research Section A: Accelerators, Spectrometers, Detectors and Associated Equipment*, 777:172–188, mar 2015.
- [24] Wolfgang R. Plaß and et al. Multiple-reflection time-of-flight mass spectrometry. *International Journal of Mass Spectrometry*, 349-350:134–144, sep 2013.
- [25] C. Hornung and et al. Complete ion identification by proton and mass number via high-resolution mass spectrometry at the (super-)frs. *GSI Sci. Rep.*, 2017.
- [26] H. Geissel and et al. The GSI projectile fragment separator (FRS): a versatile magnetic system for relativistic heavy ions. *Nucl. Instrum. Methods Phys. Res. Sect. B Beam Interact. Mater. At.*, 70(1-4):286–297, aug 1992.
- [27] W.R. Plaß and et al. The FRS ion catcher – a facility for high-precision experiments with stopped projectile and fission fragments. *Nuclear Instruments and Methods in Physics Research Section B: Beam Interactions with Materials and Atoms*, 317:457–462, dec 2013.
- [28] B. Voss and et al. The scintillation-detector equipment of the GSI projectile—fragment separator. *Nuclear Instruments and Methods in Physics Research Section A: Accelerators, Spectrometers, Detectors and Associated Equipment*, 364(1):150–158, sep 1995.
- [29] R. Janik and et al. Time projection chambers with c-pads for heavy ion tracking. *Nuclear Instruments and Methods in Physics Research Section A: Accelerators, Spectrometers, Detectors and Associated Equipment*, 640(1):54–57, jun 2011.
- [30] M. Pfützner and et al. Energy deposition by relativistic heavy ions in thin argon absorbers. *Nuclear Instruments and Methods in Physics Research Section B: Beam Interactions with Materials and Atoms*, 86(3-4):213–218, apr 1994.
- [31] A. Stolz and et al. A detector system for the identification of relativistic heavy ions at high rates. *GSI Scientific Report*, page 174, 1998.

- [32] E. Hanelt. Study of the momentum loss achromate and its application to the measurement of the β -delayed neutron radioactivity of ^{14}Be , ^{17}B , and ^{19}C . *PhD thesis Darmstadt, Techn. Hochschule*, 1992.
- [33] Maria Goeppert Mayer. On closed shells in nuclei. II. *Physical Review*, 75(12):1969–1970, jun 1949.
- [34] Otto Haxel and et al. On the "magic numbers" in nuclear structure. *Physical Review*, 75(11):1766–1766, jun 1949.
- [35] S. G. Nilsson. *Dan. Mat. Fys. Medd* 16, 29, 1955.
- [36] F. Iachello and A. Arima. The interacting boson model. aug 1987.
- [37] R. F. Casten. Shape phase transitions and critical-point phenomena in atomic nuclei. *Nature Physics*, 2(12):811–820, dec 2006.
- [38] Meng Wang and et al. The AME 2020 atomic mass evaluation (II). tables, graphs and references. *Chinese Phys C*, 45(3):030003, mar 2021.
- [39] A. Spătaru. Extension of the particle identification at the gsi fragment separator by high-resolution mass spectrometry. *Master Thesis*, 2016.
- [40] Meng Wang and et al. The AME2016 atomic mass evaluation (II). tables, graphs and references. *Chinese Physics C*, 41(3):030003, mar 2017.
- [41] Ashok Kumar Jain and et al. Atlas of nuclear isomers. *Nuclear Data Sheets*, 128:1–130, sep 2015.
- [42] A. Spătaru and et al. First coupling of the FRS particle identification and the FRS-ion catcher data acquisition systems: The case of ^{109}In . *Nucl Instrum Methods Phys Res Sect B Beam Interact Mater At*, 522:32–37, jul 2022.
- [43] G. Audi and et al. The NUBASE2016 evaluation of nuclear properties. *Chinese Physics C*, 41(3):030001, mar 2017.
- [44] Samuel Ayet San Andrés and et al. High-resolution, accurate multiple-reflection time-of-flight mass spectrometry for short-lived, exotic nuclei of a few events in their ground and low-lying isomeric states. *Physical Review C*, 99(6):064313, jun 2019.
- [45] A. Spătaru and et al. Nuclear structure studies with high-precision mass measurements of spontaneous fission fragments at the FRS ion catcher. *Bulgarian Journal of Physics*, 48(5-6):535–540, dec 2021.
- [46] T. Dickel and et al. Multi-nucleon transfer reactions at ion catcher facilities - a new way to produce and study heavy neutron-rich nuclei. *J. Phys.: Conf. Ser.*, 1668(1):012012, oct 2020.
- [47] A. Spătaru and et al. Study of exotic nuclei produced in multinucleon transfer reactions at the igisolfacility. *ELI-NP Annual Report*, 2022.
- [48] A. Spătaru and et al. Multi-nucleon transfer reactions in $^{238}\text{U}+^{64}\text{Ni}$ using grazing model. *U.P.B. Sci. Bull., Series A*, 82(1):285, 2020.
- [49] A. Spătaru and et al. Accurate mass measurements near the $n=90$ shape phase transition region at the frs-ic. *in progress*, 2023.
- [50] N. Minkov and et al. K-isomeric states in well-deformed heavy even-even nuclei. *Physical Review C*, 105(4):044329, apr 2022.
- [51] D.L. Balabanski and et al. Photofission experiments at ELI-NP. *Romanian Reports in Physics*, 68(Supplement):S621–S698, 2016.